Draft version January 22, 2019
Preprint typeset using LaTeX style emulateapj v. 01/23/15

arXiv:1710.09329v1 [astro-ph.GA] 25 Oct 2017

RELICS: STRONG LENS MODELS FOR FIVE GALAXY CLUSTERS FROM THE REIONIZATION LENSING CLUSTER SURVEY

Catherine Cerny[1], Keren Sharon[1], Felipe Andrade-Santos[2], Roberto J. Avila[3], Maruša Bradač[4], Larry D. Bradley[3], Rychard J. Bouwens[5], Daniela Carrasco[6], Dan Coe[3], Nicole G. Czakon[7], William A. Dawson[8], Brenda L. Frye[9], Austin T. Hoag[4], Kuang-Han Huang[4], Traci L. Johnson[1], Christine Jones[2], Daniel Lam[5], Lorenzo Lovisari[2], Ramesh Mainali[9], Pascal A. Oesch[10], Sara Ogaz[3], Matthew Past[1], Rachel Paterno-Mahler[1], Avery Peterson[1], Adam G. Riess[3], Steven A. Rodney[11], Russell E. Ryan[3], Brett Salmon[3], Irene Sendra-Server[12], Daniel P. Stark[9], Louis-Gregory Strolger[3], Michele Trenti[6], Keiichi Umetsu[7], Benedetta Vulcani[6], Adi Zitrin[13]

Draft version January 22, 2019

ABSTRACT

Strong gravitational lensing by galaxy clusters magnifies background galaxies, enhancing our ability to discover statistically-significant samples of galaxies at $z > 6$, in order to constrain the high-redshift galaxy luminosity functions. Here, we present the first five lens models out of the Reionization Lensing Cluster Survey (RELICS) Hubble Treasury Program, based on new *HST* WFC3/IR and ACS imaging of the clusters RXC J0142.9+4438, Abell 2537, Abell 2163, RXC J2211.7−0349, and ACT−CLJ0102−49151. The derived lensing magnification is essential for estimating the intrinsic properties of high-redshift galaxy candidates, and properly accounting for the survey volume. We report on new spectroscopic redshifts of multiply imaged lensed galaxies behind these clusters, which are used as constraints, and detail our strategy to reduce systematic uncertainties due to lack of spectroscopic information. In addition, we quantify the uncertainty on the lensing magnification due to statistical and systematic errors related to the lens modeling process, and find that in all but one cluster, the magnification is constrained to better than 20% in at least 80% of the field of view, including statistical and systematic uncertainties. The five clusters presented in this paper span the range of masses and redshifts of the clusters in the RELICS program. We find that they exhibit similar strong lensing efficiencies to the clusters targeted by the Hubble Frontier Fields within the WFC3/IR field of view. Outputs of the lens models are made available to the community through the Mikulski Archive for Space Telescopes.

Subject headings: galaxies: clusters: individual (RXCJ0142.9+4438, Abell2537, Abell2163, RXCJ2211.7-0349, ACT-CLJ0102-49151) — gravitational lensing: strong

1. INTRODUCTION

The search for high-redshift galaxies is central to the study of early galaxy formation and evolution. The galaxy luminosity function can be used as a tool to determine the distribution and statistical properties of galaxies throughout the universe over cosmic time, and can lend insight into the early stages of galaxy evolution. However, constraining this function is challenging at redshifts greater than $z \sim 9$ (Bouwens et al. 2015). This time period marks the epoch of reionization (*Planck* Collaboration 2016, Robertson et al. 2015), which is not yet well understood owing to the small number of sources that have been detected at such high redshifts. Due to cosmological dimming, without lensing magnification most observable high-redshift galaxies are drawn from the luminous end of the luminosity function, and are thus not representative of their population.

The Reionization Lensing Cluster Survey (RELICS; Coe et al., in preparation) seeks to discover a statistically significant sample of galaxies at high redshifts, in order to better constrain the luminosity functions and improve subsequent study of the epoch of reionization. It aims to achieve this scientific goal by combining the high resolution and infrared capabilities of *HST* with the magnification boost of strong gravitational lensing by galaxy clusters. Contrary to extremely deep lensing program such as the Hubble Frontier Fields (Lotz et al. 2017), RELICS maximizes the probability of discovering galaxies at high redshift by conducting relatively shallow observations of a large area. Our 190-orbit *HST* Trea-

---

krosah@umich.edu
[1] Department of Astronomy, University of Michigan, 1085 South University Ave, Ann Arbor, MI 48109, USA
[2] Harvard-Smithsonian Center for Astrophysics, 60 Garden Street, Cambridge, MA 02138, USA
[3] Space Telescope Science Institute, 3700 San Martin Drive, Baltimore, MD 21218, USA
[4] Department of Physics, University of California, Davis, CA 95616, USA
[5] Leiden Observatory, Leiden University, NL-2300 RA Leiden, The Netherlands
[6] School of Physics, University of Melbourne, VIC 3010, Australia
[7] Institute of Astronomy and Astrophysics, Academia Sinica, PO Box 23-141, Taipei 10617,Taiwan
[8] Lawrence Livermore National Laboratory, P.O. Box 808 L-210, Livermore, CA, 94551, USA
[9] Department of Astronomy, Steward Observatory, University of Arizona, 933 North Cherry Avenue, Rm N204, Tucson, AZ, 85721, USA
[10] Department of Astronomy, Yale University, New Haven, CT 06520, USA
[11] Department of Physics and Astronomy, University of South Carolina, 712 Main St., Columbia, SC 29208, USA
[12] Infrared Processing and Analysis Center, California Institute of Technology, MS 100-22, Pasadena, CA 91125
[13] Physics Department, Ben-Gurion University of the Negev, P.O. Box 653, Beer-Sheva 84105, Israel

TABLE 1
Cluster Properties

Cluster	R.A. (J2000)	Dec (J2000)	z	Mass ($10^{14} M_\odot$)
Abell 2537	23:08:21	−02:11:44	0.2966	5.52
RXC J0142.9+4438	01:42:53	44:38:20	0.3410	9.02
RXC J2211.7-0349	22:11:43	−03:49:45	0.3970	10.50
ACT-CLJ0102-49151	01:02:56	−49:16:18	0.8700	10.75
Abell 2163	16:15:49	−06:09:08	0.2030	16.12

Note. — Clusters considered in this work. The mass estimate is M_{500} from *Planck* Collaboration (2015).

sury Program (GO 14096; PI Coe) observed 41 clusters with ACS and WFC3/IR, providing the first *HST* infrared images of these fields. Additionally, 390 hours of Spitzer imaging (PI Bradač, PI Soifer) support the high redshift search and help constrain galaxy properties.

To fully exploit the strong lensing boost of the foreground galaxy clusters, one must determine the lensing potential of each cluster, by computing a detailed lens model that determines the projected mass density distribution of the lensing cluster. The derived lensing magnification is required for converting observed measurements such as size, luminosity, star formation rate, and stellar mass of lensed galaxies to their intrinsic physical properties. Additionally, the lens models provides a magnification correction for the survey volume, which is used to normalize the luminosity functions. RELICS will publish lens models for each strong lensing cluster, based on the observed locations of strongly lensed, multiply imaged, background galaxies. The redshift of these lensed galaxies is especially important for the accuracy of the models, as inaccurate redshifts can significantly bias the derived magnification (Johnson & Sharon, 2016). We employ ground-based spectroscopic observations in conjunction with *HST* photometry in order to better constrain our lens models.

The lens modeling community has taken an increasingly serious look at systematic biases in recent years. In this paper, we continue this effort by investigating the systematic uncertainties due to lack of spectroscopic redshifts of lensed galaxies; we detail our new strategy for reducing lens modeling bias by a careful incorporation of the photometric redshift posterior into the lens modeling process.

Here, we present strong lens models for five clusters from the first set of RELICS Cycle 24 observations. We describe the sample selection in Section 2, and the *HST* imaging and ground-based spectroscopy followup in Section 3. We then describe the lens modeling process we used and show the lens models and best-fit parameters in Section 4. We assess the lens modeling uncertainties in Section 5. Finally, in Section 6, we discuss our results and consider how our methods can be applied to future work in this survey and beyond. We assume ΛCDM cosmology throughout this paper with Ω_M=0.3, Ω_Λ=0.7, and H_0 =70 km s^{-1} Mpc^{-1}. All magnitudes are measured in the AB system. We use the standard notation M_Δ to denote the mass enclosed within a sphere of r_Δ, within which the mean overdensity equals $\Delta \times \rho_c$ with ρ_c the critical density of the universe at the cluster redshift. All images are oriented North-East.

2. SAMPLE SELECTION

The RELICS program observed a total of 46 fields lensed by 41 galaxy clusters, with a selection based on their Sunyaev Zel'dovich effect (SZ) or Xray-inferred mass and other criteria. The sample will be described in full detail in a forthcoming paper (Coe et al., in prep).

About half of the RELICS clusters were mass-selected from the *Planck* SZ cluster catalog (*Planck* Collaboration 2014). The *Planck* cluster catalog provides redshifts and mass estimates for 1094 clusters. Of the 34 most massive clusters ($M_{500} > 8.8 \times 10^{14} M_\odot$), only 13 have already been imaged by *HST* in the IR prior to Cycle 23. The remaining 21 clusters form our mass-selected sample. These clusters are expected to have X-ray masses similar to or greater than clusters in the Frontier Fields program (Lotz et al. 2017) and the CLASH program (Postman et al. 2012); the average mass in CLASH is $M_{500} \simeq 1.0 \times 10^{15} M_\odot h_{70}^{-1}$ (Umetsu et al. 2014, 2016), and the lowest M_{500} mass is $4 - 5 \times 10^{14} M_\odot h_{70}^{-1}$. High mass clusters are likely to have a large cross-section for strong lensing, making them ideal candidates for the survey.

To increase the efficiency of the program, the other 20 clusters were selected as clusters that have previously been identified as prominent strong lenses based on available imaging. The selection of these 20 clusters also relied on X-ray mass estimates (MCXC compilation Piffaretti et al. 2011; Mantz et al. 2010); weak lensing mass estimates (Sereno et. al 2015 compilation, including Weighing the Giants, Applegate et al. 2014, von der Linden et al. 2014; Umetsu et al. 2014; Hoekstra et al. 2015); and SZ mass estimates from SPT (Bleem et al. 2015) and ACT (Hasselfield et al. 2013). We also considered a range of clusters from the SDSS survey (Wong et al. 2013, Wen et al. 2012) and clusters nearly selected for the Frontier Fields. The survey design thus maximizes the chances of finding high redshift galaxies.

The clusters presented in this paper (Table 1) are the first five clusters with completed models. Lens models for the remaining 36 cluster fields will be presented in future papers.

3. OBSERVATIONS

3.1. *HST Imaging*

We obtained optical and near-infrared HST photometric data of 41 galaxy cluster fields with the Wide Field Camera 3 (WFC3) and the Advanced Camera for Surveys (ACS). We use four WFC3/IR filters and three ACS filters, which span the wavelength range of $0.4 - 1.7$ microns. These filters are used over a total of 190 orbits to

TABLE 2
Cluster Imaging Parameters

Cluster	Filter	Date of Observation	Exposure time [s]	PID
Abell 2537	ACS F435W	2016-06-08	2162	RELICS
	ACS F606W	2002-10-02	2080	GO9270
	ACS F814W	2016-07-19	2162	RELICS
	WFC3/IR F105W	2016-07-19	756	RELICS
		2016-08-06	756	RELICS
	WFC3/IR F125W	2016-07-19	356	RELICS
		2016-08-06	356	RELICS
	WFC3/IR F140W	2016-07-19	356	RELICS
		2016-08-06	356	RELICS
	WFC3/IR F160W	2016-07-19	1006	RELICS
		2016-08-06	956	RELICS
RXC J0142.9+4438	ACS F435W	2015-12-04	2268	RELICS
	ACS F606W	2016-01-14	2189	RELICS
	ACS F814W	2015-12-04	2439	RELICS
	WFC3/IR F105W	2015-12-04	756	RELICS
		2016-01-14	756	RELICS
	WFC3/IR F125W	2015-12-04	356	RELICS
		2016-01-14	406	RELICS
	WFC3/IR F140W	2015-12-04	381	RELICS
		2016-01-14	406	RELICS
	WFC3/IR F160W	2015-12-04	1106	RELICS
		2016-01-14	956	RELICS
RXC J2211.7-0349	ACS F435W	2016-11-25	1953	RELICS
	ACS F606W	2011-11-19	1200	GO12166
		2015-11-25	2101	RELICS
	ACS F814W	2016-11-25	2124	RELICS
	WFC3/IR F105W	2015-10-16	706	RELICS
		2015-11-25	706	RELICS
	WFC3/IR F125W	2015-10-16	356	RELICS
		2015-11-25	356	RELICS
	WFC3/IR F140W	2015-10-16	331	RELICS
		2015-11-25	356	RELICS
	WFC3/IR F160W	2015-10-16	906	RELICS
		2015-11-25	1006	RELICS
ACT-CLJ0102-49151	ACS F435W	2016-07-08	2093	RELICS
	ACS F606W	2012-12-22	1920	GO12477
	WFC3/IR F105W	2016-07-09	706	RELICS
		2016-08-08	756	RELICS
	WFC3/IR F125W	2016-07-09	356	RELICS
		2016-08-08	381	RELICS
	WFC3/IR F140W	2016-07-09	356	RELICS
		2016-08-08	381	RELICS
	WFC3/IR F160W	2016-07-09	1006	RELICS
		2016-08-08	1006	RELICS
Abell 2163	ACS F435W	2011-07-03	4664	GO12253
	ACS F606W	2011-07-03	4667	GO12253
	ACS F814W	2011-07-03	9192	GO12253
	WFC3/IR F105W	2016-09-03	706	RELICS
		2016-04-18	706	RELICS
	WFC3/IR F125W	2016-09-03	356	RELICS
		2016-04-18	356	RELICS
	WFC3/IR F140W	2016-09-03	356	RELICS
		2016-04-18	356	RELICS
	WFC3/IR F160W	2016-09-03	1006	RELICS
		2016-04-18	1006	RELICS

Note. — Dates, filters, and exposure times for each cluster, including both RELICS observations and archival data from other proposals.

image 46 fields lensed by 41 clusters.[14] Each cluster was observed for a total of five orbits, except for cases where archival data from the ACS are available. In these cases, the number of orbits was reduced accordingly. Each cluster was observed in two epochs separated by $40-60$ days in order to identify supernovae and other transient phenomena. Table 2 lists the observing dates and exposure times for RELICS observations of the fields considered in this work, and provides the proposal identification information for archival data.

TABLE 3
Cluster Spectroscopy Observations

Cluster	Date	Exposure Time, Notes
Abell 2163	2016 Jun 07-08	1h
Abell 2537	2016 Aug 02-03	2 masks, 1.5h each
RXC J2211.7-0349	2016 Aug 02-03	2h
ACT-CLJ0102-49151	2016 Aug 02-03	2h

Note. — Dates and exposure times for spectroscopic observations carried out with Magellan/LDSS3 on the clusters presented in this paper to date.

---

[14] 20 of the orbits are designated as ToO to follow-up lensed supernova candidates.

3.2. *Imaging Data Reduction*

All sub-exposures in each filter were combined to form a deep image using the AstroDrizzle package (Gonzaga et al. 2012) using `PIXFRAC`=0.8. The data in different filters were aligned to the same pixel frame, and the astrometry was corrected to match the Wide-field Infrared Survey Explorer (WISE) point source catalog (Wright et al. 2010). Final drizzled images were generated in two pixel scales: $0\farcs03$ and $0\farcs06$, for best sampling of the ACS and WFC3/IR point spread functions, respectively. The ACS data were corrected for charge transfer inefficiency losses prior to drizzling. The final reduced data are made available to the public as high level science products through the Mikulski Archive for Space Telescopes (MAST).[15]

3.3. *Photometry Catalog*

The RELICS team produces catalogs of photometry and photometric redshifts for each field, based on the final $0\farcs06$ dataset, also made available through MAST. A full description of the photometry data products will appear in a separate publication (Coe et al., in preparation). Sources are extracted from weighted stack of all the data (ACS and WFC3/IR), and from the weighted stacked WFC3/IR data alone using SExtractor (Bertin & Arnouts 1996) version 2.8.6 in dual-image mode. The weighted stack image is used as the reference image in SExtractor for all seven filters. Their fluxes and colors are measured within isophotal apertures, and corrected for Galactic extinction (Schlafly & Finkbeiner 2011).

The photometric redshift (photo-z) of each galaxy is estimated using the BPZ algorithm (Bayesian Photometric Redshifts; Benitez et al. 2000, 2014; Coe et al. 2006). We run BPZ with 11 spectral energy distribution (SED) model templates (five ellipticals, two late types, and four starbursts) as described in Benitez et al. (2014) and Rafelski et al. (2015). The models are based on PEGASE including emission lines (Fioc & Rocca-Volmerange 1997), then recalibrated to match the observed photometry of galaxies with spectroscopic redshifts from FIREWORKS (Wuyts et al. 2008). BPZ redshifts these SEDs, fitting to the observed photometry of each galaxy, using a Bayesian prior on redshift given the i-band magnitude and spectral type. The elliptical templates for galaxies at high redshifts are downweighted by the prior, and lower redshift solutions are generally preferred over those at higher redshifts. Possible lensing magnification is not considered in the prior.

Strongly lensed galaxies, in particular those used as constraints in this paper, were further inspected manually. We find that some sources yield less reliable photometric redshifts because they are fainter and/or contaminated by brighter nearby galaxies (usually cluster members). Therefore the photometric redshifts of multiple lensed images match one another often but not always. The system photo-z was manually determined by examining the redshift solution of all the images of the same system, giving higher weight to images that are brighter and better isolated. For systems that have secure identification as lensed sources (i.e., the source is behind the cluster) we excluded any redshift solutions that are lower than the cluster redshift.

3.4. *Ground-Based Spectroscopy*

Ground-based spectroscopic observations of RELICS clusters were conducted using the upgraded Low Dispersion Survey Spectrograph (LDSS3-C[16]) on the Magellan Clay telescope using University of Michigan allocation (PI: Sharon) and University of Arizona allocation (PI: Stark). We designed multi-object slit masks, with slits placed on candidate lensed galaxies at highest priority, and the remaining slits placed on cluster member galaxies (selected by color) or other interesting objects in the cluster field, such as candidate ram-pressure stripping galaxies (e.g., Ebeling et al. 2014) or candidate supernova hosts. We used the VPH-ALL grism, which has high sensitivity over the widest range of wavelengths: 4250 Å$< \lambda <$10000 Å, useful for identification of emission lines at unknown redshifts. A $1\farcs0$ slit was used for all objects, yielding a spectral resolution of R 450-1100 across that wavelength range[17]. The detector covers a spatial extent of 6.4 arcmin.

Table 3 provides the observing date and exposure time for each field considered in this work. The spectroscopic data were reduced using the standard procedures using the COSMOS data reduction package.[18] We report here on spectroscopic redshifts that were secured for candidate lensed galaxies and used as constraints in this paper. A full description of the results from these follow-up programs will be given in a future publication.

4. STRONG LENSING ANALYSIS

We present the lens models for five galaxy clusters in the RELICS survey. The properties of these clusters are given in Table 1.

Strong lens models were computed using `Lenstool` (Jullo et al. 2007), which models the cluster projected mass density as a combination of parametric halos. Each halo is modeled as pseudo-isothermal ellipsoidal mass distribution (PIEMD; Limousin et al. 2005) and the best-fit set of parameters is found using Markov Chain Monte Carlo (MCMC) sampling. Optimization for the models presented in this paper were performed in the image plane. The parameters that are allowed to vary in the modeling process, for each halo, are the x and y position of the center of the halo; the ellipticity of the halo, e; its position angle, θ; the core radius, r_{core}; and the effective velocity dispersion, σ. The truncation radius of the cluster halo was fixed at r_{cut} = 1500 kpc, as it is typically too far from the projected radii of the lensing constraints and therefore cannot be constrained by the strong lensing evidence.

Cluster-member galaxies were selected using the cluster red sequence method (Gladders & Yee, 2000), and modeled as PIEMD halos. The core radius of the cluster member galaxies was fixed at 0.15 kpc, and r_{cut} and σ were scaled with luminosity following Limousin et al. (2005). The positional parameters (x, y, e, θ) were fixed to the properties of their light distribution as measured with SExtractor (Bertin et al. 1996).

---

[15] https://archive.stsci.edu/prepds/relics/

[16] http://www.lco.cl/telescopes-information/magellan/instruments/ldss-3

[17] http://www.lco.cl/telescopes-information/magellan/instruments/specs/LDSS-3%20Handout.pdf

[18] http://code.obs.carnegiescience.edu/cosmos

The process of creating a lens model relies on the identification of multiply-imaged systems ("arcs") that are used as constraints. Arcs are identified by eye as multiple images of the same background galaxy, based on their morphology, structure, and color. When we identify a system of arcs, we verify that the orientation and parity of each arc is consistent with the expectation from lensing.

As was shown by several authors (e.g., Smith et al. 2009, Johnson & Sharon 2016), even with excellent positional constraints such as the ones provided by *HST* imaging, the accuracy of strong lens models relies on the availability of redshift information of the lensed galaxies. In particular, models that lack redshift constraints are limited in their ability to correctly measure the slope of mass distribution; the lensing magnification derived from such models may be biased (Johnson & Sharon 2016). The RELICS programs aims to provide the community with the best available lens models of these clusters in time for preparation of JWST observations. However, at the time some of these models are released some clusters in this survey have no redshift constraints, some have only a spectroscopic redshift of only one lensed galaxy, and some have two or more. In lieu of spectroscopic redshifts, one can use photometric redshifts, by setting limits on the redshift parameter based on the probability distribution function of the photometric redshift analysis. However, catastrophic outliers might bias the result, as shown in Johnson & Sharon (2016), and force the model into a wrong solution. It is therefore advised that lens models that are not based on spectroscopic redshift should be treated with caution.

To facilitate the release of lens models for all targeted clusters, including those with limited redshift constraints, we follow the procedure below when computing the lens models. The procedure aims to reduce the systematic error due to redshift uncertainty, reduce the probability of a catastrophic photo-z outlier affecting the result, and to estimate the effect of the redshift uncertainty on deliverables such as lensing magnification and mass.

Case 1 – clusters with at least one spectroscopic redshift of multiply-imaged lensed background source (Abell 2537, RXC 2211): in this case, we use the spectroscopic redshift(s) as fixed constraint(s). Arcs that do not have spectroscopic redshifts have their redshifts treated as free parameters. We test using the photometric redshift as a guide to set the redshift prior on the lens model. However, following the recommendations of Johnson & Sharon (2016), we allow broader limits than the photometric redshift probability distribution function so as not to be biased by catastrophic outliers.

Case 2 – clusters with no spectroscopic redshifts of background sources (RXC 0142, ACT 0102, Abell 2163): in this case, we attempt to leave all the redshifts as free parameters. If this approach fails (e.g., results in unrealistic model-predicted redshifts or lensing mass), we fix the redshift of one of the lensed systems to its best-fit photo-z. We test that the choice of which source to fix has minor affect on other model choices. The redshifts of the remaining sources are left as free parameters, as in Case 1.

In both cases, we test the agreement between the model-predicted redshifts (model-z) and the photo-z posterior, and require that for a viable lens model there would not be a significant systematic bias between model-z and photo-z, i.e., that the agreement between model-z and photo-z is within the 1σ uncertainties for most sources. In Section 5, we quantify the effect of the redshift parameter on the uncertainties.

In the following sections, we describe each model in more detail; the results of the lens models are given in Table 4. In all the models, our numbering scheme of multiply lensed galaxies designates the source number first, to the left of the decimal point, and the image number to the right of the decimal point. For example, three images of source galaxy #1 would be labeled 1.1, 1.2, and 1.3. Tables 5–14 give the details of the lensed galaxies that were used as constraints and the parameters for each lens model. We list IDs, coordinates, and photo-z, of each image. Spectroscopic redshift is given for sources for which those were measured; photometric redshifts are shown separately for the individual clumps that compose the same source.

4.1. *Abell 2537*

We detect four lensed systems in the field of Abell 2537, as described below (see also Table 5).

System #1 is lensed into four images. We identify three separate emission knots in this galaxy, designated as 1.1-1.4, 11.1-11.4, 12.1-12.4 in Figure 1.

System #2 is lensed into four multiple images, each one containing two emission knots. The images are labeled 2.1-2.4, 20.1-20.4 in Figure 1. We measure a spectroscopic redshift of $z_{spec} = 3.611$ for image 2.4, based on Lyα emission in our LDSS3 spectroscopy (Section 3.4). This falls within the 95% CL range of the photometric redshifts of the image and is slightly lower than its highest probability peak (Table 5). We used the spectroscopic redshift as a fixed constraint in our lensing analysis.

System #3 has three multiple images. We identify three distinct emission knots in each image, labeled 3.1-3.3, 30.1-30.3, 31.1-31.3 in Figure 1. We find that not fixing a second redshift parameter in this cluster (in addition to the one spectroscopic redshift) causes the model to default to a non-physical result, e.g. the model predicts redshifts higher than $z = 13$. We therefore fix the redshift of images 3.1-3.3 to the photometric redshift for this source, $z = 3.2$, in order to better constrain the lensing potential in the regions further away from the center of the cluster.

System #4 is a faint galaxy, labeled 4.1-4.2 in Figure 1. The lensing analysis predicts additional images at two other locations within the field, but their predicted magnitudes are too faint to be detected, which explains their absence from the data.

The lens model for this cluster favors a combination of two cluster-scale halos, both located close to the center of the cluster within the strong lensing regime. As described above, we include perturbation from galaxy scale halos. We allow the parameters of the cluster-scale halos to be solved for by the lens model. Table 5 lists the locations of the lensed galaxies and their redshifts. Table 6 lists the best-fit parameters of the resulting model.

4.2. *RXC J0142.9+4438*

We identify four lensed galaxies in the field of RXC J0142.9+4438. Their positions and photometric

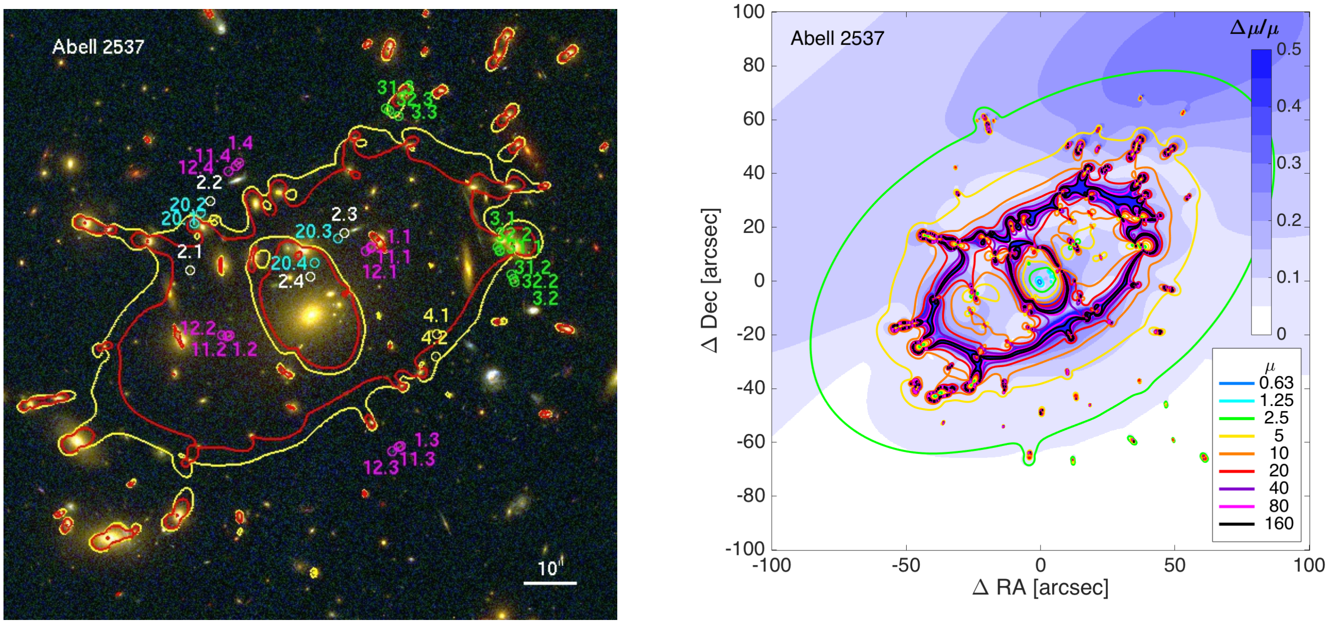

FIG. 1.— *Left*: Image of Abell 2537 created using a combination of WFC3IR imaging in the red (F160W) and ACS imaging in the green (F814W) and blue (F435W). Multiply imaged galaxies are labeled. The red curve marks the location of the critical curve for a source at $z = 3.0$. A second critical curve is plotted in yellow at $z = 9.0$. *Right*: The magnification for a source at $z = 9.0$ from the best-fit lens model is shown as contours; contour values are given in the legend. The background colormap indicates the uncertainty level in in each location, given as $\Delta\mu/\mu$. The uncertainty estimate takes into account the source redshift uncertainty, but does not account for other systematics (see text).

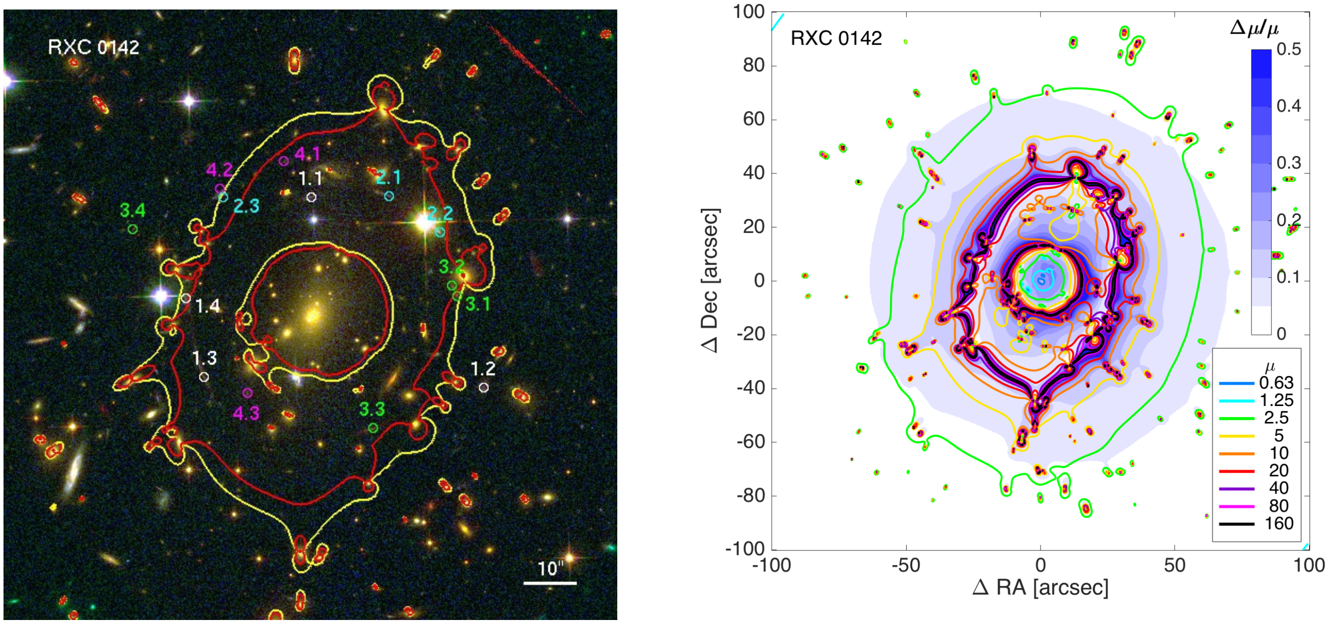

FIG. 2.— *Left*: Image of RXC J0142+44 created using a combination of WFC3/IR imaging in the red (F160W) and ACS imaging in the green (F814W) and blue (F435W) filters. The locations of multiply imaged lensed galaxies are overplotted and labeled. The red curve marks the location of the critical curve for a source at $z = 3.0$. The yellow curve marks the location of the critical curve at $z = 9.0$. *Right*: The magnification for a source at $z = 9.0$ from the best-fit lens model is shown as contours; contour values are given in the legend. The background colormap indicates the uncertainty level in in each location, given as $\Delta\mu/\mu$. The uncertainty estimate takes into account the source redshift uncertainty, but does not account for other systematics (see text).

redshifts are listed in Table 7. No spectroscopic redshifts are available for the cluster.

System #1 is labeled 1.1-1.4 in Figure 2. The photometric redshift for this system varies significantly between the four images, due to contamination from objects near images 1.3 and 1.4. The photometry of images 1.1 and 1.2 is not affected by surrounding objects and they are thus used to pinpoint a suitable photometric redshift for the system, with a photo-z around $z = 1.8$. The confidence interval of this system is formally $[0.05 - 3.86]$, however, the range below $z = 0.34$ is ruled out, since the galaxy must be behind the cluster to be lensed.

System #2 consists of one galaxy lensed three times, labeled 2.1-2.3. Due to contamination from nearby sources or low signal to noise, we were unable to measure a reliable photometric redshift for this system. We therefore set a broad prior on its redshift.

System #3 is also lensed four times, labeled 3.1-3.4. We fix the redshift of the system to $z = 3.1$ in order to constrain the redshifts of the other systems in the field. We discuss the implication of this approach in Section 5.

System #4 has three visible images, labeled 4.1-4.3. One additional image is predicted to be west of 3.1 and 3.2, but its predicted magnitude is too faint to be detected in current data.

We find that one cluster-scale halo plus galaxy-scale halos are sufficient to reproduce the lensing observables. Table 7 lists the locations of the images of the lensed galaxies and their redshifts. Table 8 lists the best-fit parameters of the resulting model.

4.3. *RXC J2211.7-0349*

We detect two lensed galaxies in the field of RXC J2211.7-0349. Their positions and photometric redshifts are listed in Table 5.

System #1 is lensed by the cluster into five multiple images, labeled 1.1-1.5 in Figure 3. We note that the demagnified image 1.5, located close to the BCG, is clearly detected in the data, and its colors and morphology match the other images. Its blue color distinguishes it from the BCG light. Images 1.1 and 1.2 were targeted for spectroscopy using a multi-object slit mask with LDSS3 on Magellan, which resulted in spectroscopic redshift of $z_{spec} = 1.051$ based on emission lines from [OII], [NeIII] 3869, and H_β. The photometric redshifts of these images favor a lower redshift, with 95% CL range of $[0.821 - 0.979]$ and highest likelihood at $z_{phot} = 0.85$. The spectroscopic redshift is outside the 95% CL, but has non-zero BPZ probability for the observed z_{spec}. In the lensing analysis of this cluster we use the spectroscopic redshift of source #1 as a fixed constraint.

System #2 and system #3 are lensed into three images labeled 2.1-2.3, 3.1-3.3, respectively. System #3 was targeted for spectroscopy; however, we were unable to secure a spectroscopic redshift from the data.

We identify an Einstein Cross configuration around a galaxy $90''.2$ from the cluster core at *R.A.*=22:11:41.986, *Decl.*=-03:50:52.31. The F606W-F814W color of the lensing galaxy is redder than the cluster red sequence, likely placing this lens galaxy behind the cluster. The lensing potential of this galaxy is boosted by the nearby lensing potential of the cluster, thus allowing it to reach a critical mass density for strong lensing. The projected distance of this lensing galaxy is far enough from the center of the cluster that it does not significantly affect the cluster lensing potential. We therefore exclude this galaxy and lensed images from the model and leave an analysis of this lensing galaxy to future work.

We find that two cluster-scale halos are required in order to match the lensing observables, supplemented by galaxy-scale halos. Table 9 lists the locations of the lensed galaxies and their redshifts. Table 10 lists the best-fit parameters of the resulting model. The projected mass density of this cluster appears to be a "warped" elliptical, with a radius-dependent position angle. This may indicate a more complex dark matter distribution than what may be implicated from the galaxy distribution. A multiwavelength and dynamical analysis of this cluster may shed more light on its structure.

4.4. *ACT-CLJ0102-49151*

We identify nine lensed systems in the field of ACT-CLJ0102-49151, also known as "El Gordo" (Menanteau et al. 2012). Except where noted otherwise, the photometric redshifts for the multiple images of each system are consistent with each other, as shown in Table 11. Spectroscopy was attempted for this cluster, but no spectroscopic redshifts for any arcs were obtained.

This cluster was previously modeled by Zitrin et. al (2013; hereafter Z13), using ACS imaging data taken as part of GO-12755 (PI: Hughes), in F625W, F775W, and F850LP, and ground-based data. Z13 identifies nine systems and candidate lensed galaxies and uses them to create a Light-Traces-Mass lens model. The new *HST* imaging data confirms five of these systems, and suggest new systems. Where available, we labeled our arcs with the same designation as in Z13 for consistency. These arcs are systems #1, #2, #4, #5, and #9.

System #1 has two emission knots, labeled 1.1-1.3 and 10.1-10.3 in Figure 4. Arc system #1 matches the identification of Z13. Arc system #10 is a secondary emission knot in the same system, clearly resolved from #1 in the *HST* data.

System #2 appears as a straight, elongated arc, NW of the southern core of the cluster towards the northern core. The low curvature of this giant arc is indicative of significant lensing potential on both sides, as we see in the mass distribution that was derived for this cluster, as well as in other merging clusters (e.g., the "Bullet Cluster", Bradac et al. 2006; Clowe et al. 2006). We identify several distinct emission clumps in this arc, and their mapping indicates that the giant arc is a merging pair of two of the images of this system, bisected by the critical curve for its redshift. The third and much less distorted image of this source is clearly identified, and labeled 2.3 and 20.3 in accordance with the Z13 identification.

System #3 is a newly identified system with three images, labeled 3.1, 3.2, 3.3.

System #4 is labeled 4.1, 4.2, 4.3. Our lensing analysis agrees with the identification of Z13 for arcs Z13-4.1, Z13-4.4, and Z13-4.5; however, we repudiate the identification of arcs Z13-4.2 and candidate arc Z13-c4.3 as part of the same system.

The new *HST* data shows that their color is much bluer than arcs 4.1-4.3, and their predicted positions are inconsistent with our lens model.

System #5 corresponds to arc candidate c5.3 in Z13. We disagree with the predicted counter image candidate

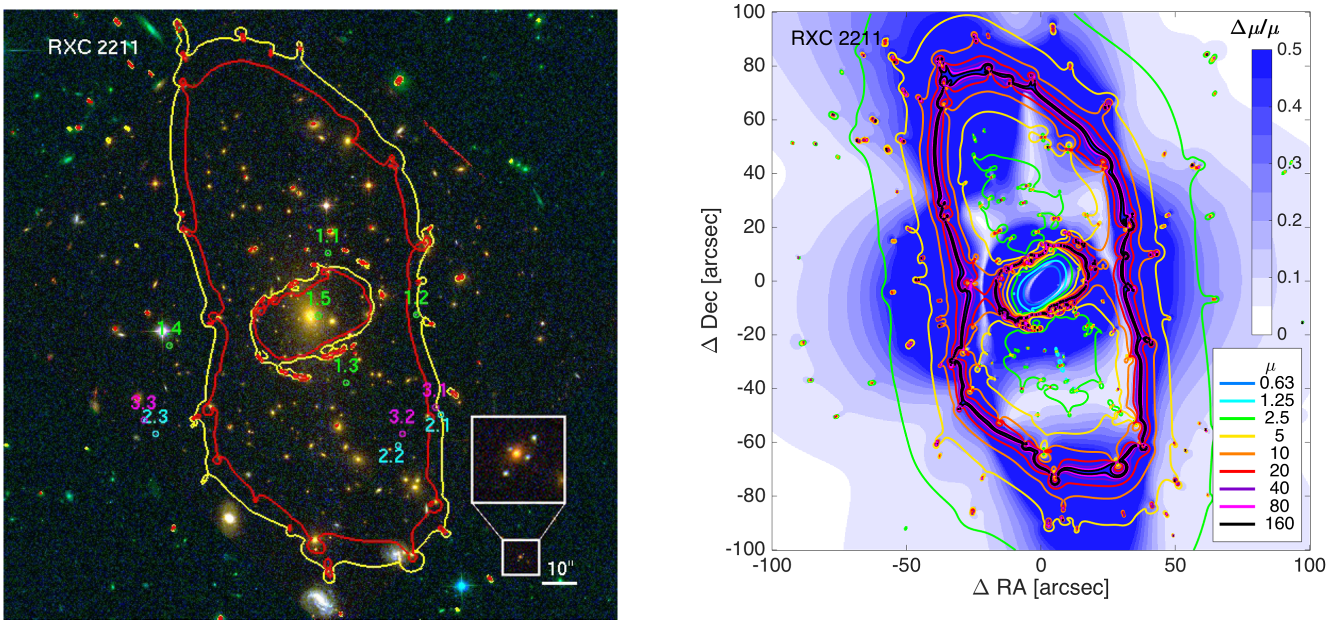

Fig. 3.— *Left*: Image of RXC J2211.7-0349, from WFC3/IR imaging in the red (F160W) and ACS imaging in the green (F814W) and blue (F435W). The locations of multiply imaged arcs are plotted and labeled. The red curve marks the location of the critical curve for a source at $z = 3.0$. The yellow curve marks the location of the critical curve at $z = 9.0$. *Right*: The magnification for a source at $z = 9.0$ from the best-fit lens model is shown as contours; contour values are given in the legend. The background colormap indicates the uncertainty level in in each location, given as $\Delta\mu/\mu$. The uncertainty estimate takes into account the source redshift uncertainty, but does not account for other systematics (see text).

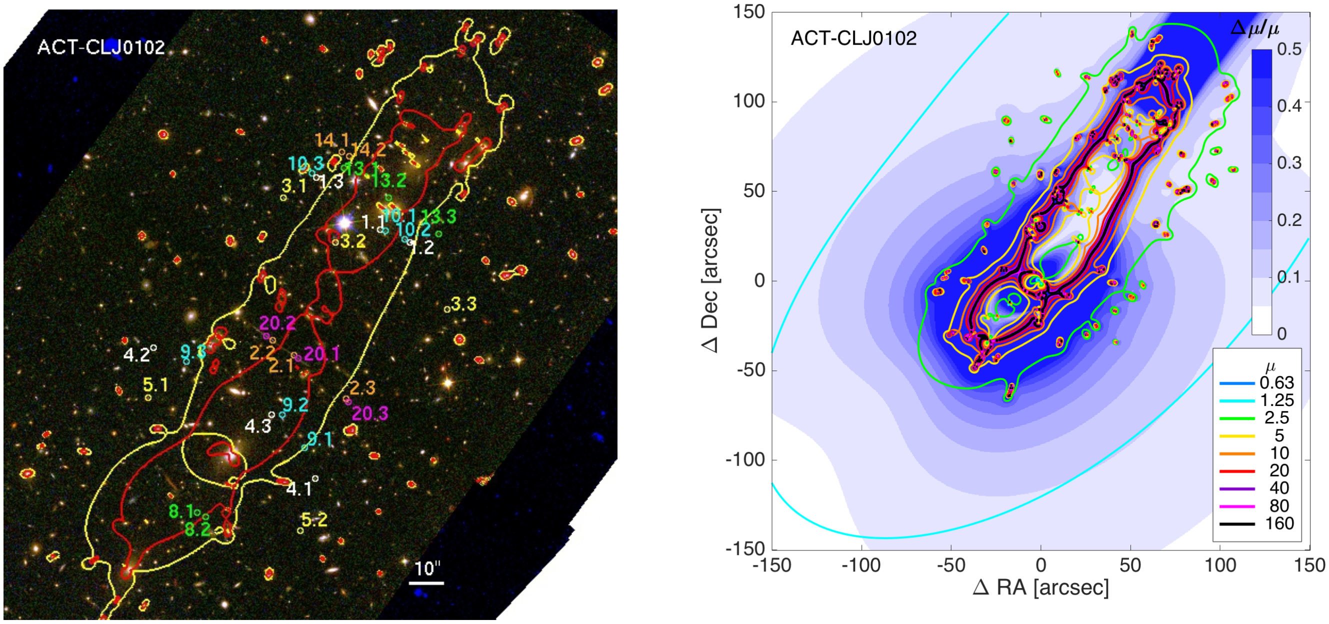

Fig. 4.— *Left*: Composite color image of ACT-CLJ0102-49151 created using a combination of WFC3IR imaging (red: F160W, green: F105W), and ACS imaging (blue: F775W). The images of lensed galaxies are overplotted and labeled. The red and yellow curves mark the location of the critical curves for a source at $z = 3.0$ and $z = 9.0$, respectively. *Right*: The magnification for a source at $z = 9.0$ from the best-fit lens model is shown as contours; contour values are given in the legend. The background colormap indicates the uncertainty level in in each location, given as $\Delta\mu/\mu$. The uncertainty estimate takes into account the source redshift uncertainty, but does not account for other systematics (see text).

c5.1/2 in Z13, and identify a new image at 5.1 based on similar parity, orientation, and colors.

System #8, labeled 8.1 and 8.2, is a new identification.

System #9, has three images; 9.1-9.2 corresponds to arc candidates c9.1 and c9.2 in Z13. We revise the position of 9.3 to be slightly more northwest of candidates c9.3 in Z13; otherwise the image identifications are the same.

System #13, labeled 13.1, 13.2, 13.3, is a new identification, made possible by its distinct IR-Visible colors.

System #14, labeled 14.1, 14.2, is also a new identification of a faint pair of arcs near the northern core of the cluster.

We find that two cluster-scale halos are needed in order to produce the lensing observables, similar to the previous model of Z13. These halos are located at the two regions that appear to have the densest galaxy distribution in the cluster, in the northern half and in the southern half of the field of view. Table 11 lists the locations of the lensed galaxies and their redshifts. Table 12 lists the best-fit parameters of the resulting model.

4.5. *Abell 2163*

Abell 2163 is the most massive cluster in the RELICS survey with an estimated *Planck* mass $M_{500} = 16.12 \times 10^{14} M_{\odot}$.

We identify four lensed galaxies near the core of Abell 2163, each with three images. They are labeled 1.1-1.3, 2.1-2.3, 3.1-3.3, 4.1-4.3 in Figure 5.

Spectroscopic observations were attempted for this cluster, however, while redshifts were obtained for several cluster member galaxies, we were unable to measure spectroscopic redshifts for any lensed galaxies used in the model.

The redshift of arc system #1 is fixed at $z = 3.0$ based on the photometric redshift measurements of arcs 1.1 and 1.2. We note that the peak of the probability distribution function of the photometric redshift of image 1.3 is much lower, at $z = 0.335$, but the redshift assumed for the system is within its 95% CL range of [0.227-3.492]. The redshift of this system is fixed (and not left as a free parameter) in order to prevent the model from converging on $z > 6$ for all the lensed systems. Such high redshifts for these lensed galaxies are unreasonable because their images are clearly detected in the F606W and F435W bands, ruling out a high redshift source.

We find that one central halo is sufficient to produce the lensing observables. Table 13 lists the locations of the lensed galaxies and their redshifts. Table 14 lists the best-fit parameters of the resulting model.

5. UNCERTAINTY ANALYSIS

Tables 6, 8, 10, 12, 14 list the best-fit model parameters and their 1σ statistical uncertainties as derived from the MCMC sampling of the parameter space. To estimate the statistical uncertainties in the magnification and mass maps, we randomly selected 100 sets of parameters from the MCMC chain, and computed the mass and magnification of each model. The statistical uncertainty is calculated as the standard deviation of values in each pixel. As explained below, this uncertainty is likely underestimating the true uncertainty of the lens modeling process.

The statistical uncertainties on the magnification are typically at a few percent level in most of the field of view, except for regions close to the critical curve. However, several sources of systematic uncertainty can contribute significantly to the error budget (e.g., Zitrin et al. 2015, Johnson et al. 2016, Meneghetti et al. 2016, Rodney et al. 2016). Below, we quantify the amplitude of the systematic uncertainty that is a direct result of our modeling choice in how to treat the redshift parameter of sources without spectroscopic redshift. Other sources of error include, e.g., mass projected along the line of sight, substructures or other correlated structures that are not accounted for (Gruen et al. 2015; Umetsu et al. 2016; Chirivì et al. 2017).

Three tests were conducted on each model in order to better quantify the uncertainties associated with the lack of spectroscopic redshift constraints. As explained in Section 4, in clusters without spectroscopic redshifts we chose one arc system with a photometric redshift close to $z = 3.0$ and fixed the redshift of that system to its photometric prediction. The redshifts of the other sources were left as free parameters, with a broad range (typically between $z_{cluster}$-8.0). We refer to this approach as “model1” hereafter.

The “model2” test left all the non-spectroscopic redshifts as free parameters, with none fixed. However, the priors on the free redshift of each system were constrained to match the photometric redshift range for each system. This range was determined by examining each photometric redshift in a system and using the lowest z_{min} and highest z_{max} values in a system as conservative lower and upper boundaries. These values were drawn from the 95% confidence interval for the photometric redshifts for each system, and thus correspond to the 2.5th and 97.5th percentile redshifts for each system.

In “model3” test, the redshift of one of the systems was fixed to its most likely photo-z as in the original model, but the priors on the free redshifts were constrained to the photometric redshift range as in model 2.

Among these three test models, model 1 has the broadest constraints on the free redshift parameters in order to account for potential photo-z outliers. We therefore use this model as the fiducial model. Comparatively, models 2 and 3 use more restrictive redshift priors. Despite the differences in the rigidity of the constraints between the three models, the final results for models 1-3 are generally consistent with each other.

We also conduct two “extreme” tests, which are designed to investigate the effect of fixing a model parameter to a significantly wrong redshift. These tests examined how the model would change if the fixed photometric redshift was shifted down to $z = 2.0$ (“testE1”) and up to $z = 4.0$ (“testE2”), while all other arcs remained free parameters.

These tests not performed on RXC 2211, which has no fixed photometric redshifts. This cluster has only two lensed systems, one of them with spectroscopic redshift. Fixing the redshift of the only other system would artificially reduce the uncertainties, and we thus left it as free parameter. Abell 2537, the second cluster in this paper with spectroscopic redshift information, has a more complex model and is richer in lensing observables. It requires two fixed redshifts to adequately constrain the strong lensing potential near its outskirts. While one of

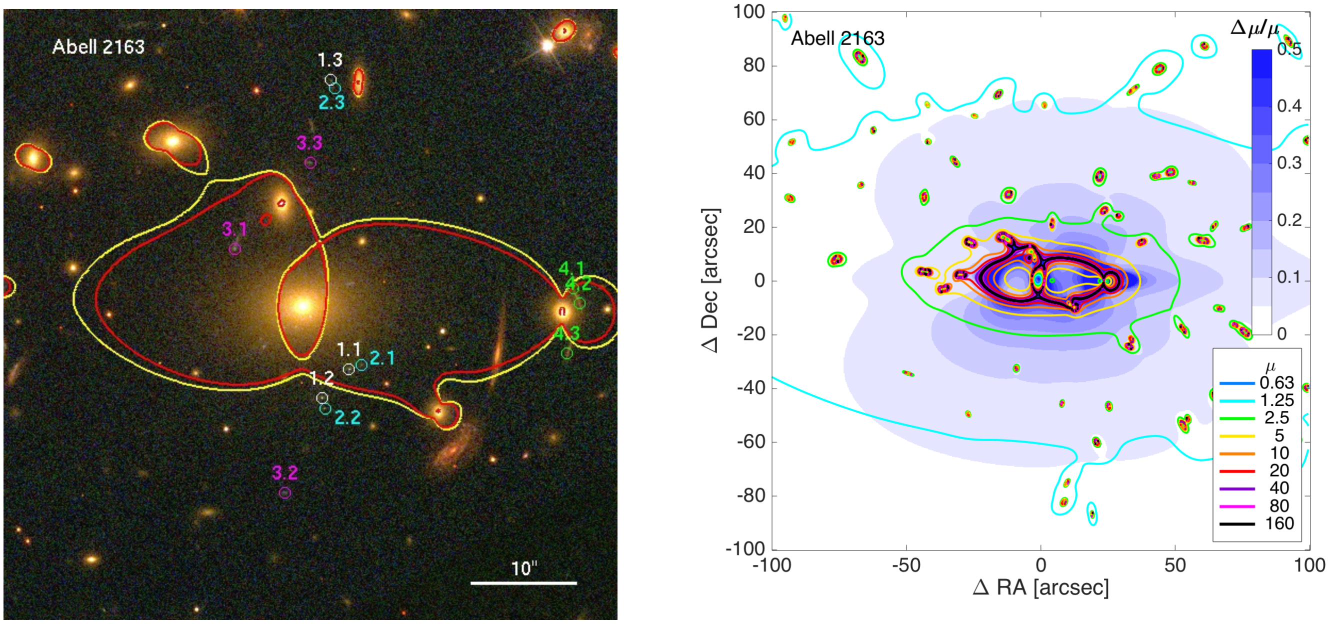

FIG. 5.— *Left*: Composite color image of Abell 2163 created using ACS imaging (red: F814W, green: F606W, blue: F435W). The images of lensed galaxies are overplotted and labeled. The locations of the critical curves for sources at $z = 3.0$ and $z = 9.0$, are marked in red and yellow, respectively. *Right*: The magnification for a source at $z = 9.0$ from the best-fit lens model is shown as contours; contour values are given in the legend. The background colormap indicates the uncertainty level in in each location, given as $\Delta\mu/\mu$. The uncertainty estimate takes into account the source redshift uncertainty, but does not account for other systematics (see text).

these fixed redshifts is the spectroscopic redshift we had acquired, the second fixed redshift is assigned its photo-z measurement. We therefore perform testE1 and testE2 on the fixed photo-z for this cluster.

Figure 6 serves as a diagnostic tool to rule out models that rely on false assumptions. For each model, we plot the model-predicted redshift of the sources against the photometric redshift measurements. We find that models that rely on an outlier redshift (i.e., testE1 and testE2 models) predict systematically low or high redshifts for other sources, compared to the photometric redshift probability distribution function. While we can expect a small fraction of photometric redshifts to be catastrophic failures, it is unlikely that *all* of them would be. We therefore argue, that we would be able to identify extremely false redshift assumption based on this diagnostic. Based on such plots, testE1 and test E2 would be ruled out as viable models, and we would be forced to revise our modeling assumptions.

For each of the test models above, we compute the lensing magnification map, and compare it to that of model1. In particular, we examine the fractional error in each pixel, as $\Delta\mu = (|\mu_{test}| - |\mu_{model1}|)/|\mu_{model1}|$. From comparing model1, model2, and model3, we find that in most cases, modifying our lens modeling choice for redshift priors changes the derived magnification at the few percent level, with no significant bias. However, this deviation is in most cases significantly higher than the statistical error of either model as derived from the MCMC sampling. This comparison indicates clearly that the MCMC statistical uncertainties underestimate the true uncertainty due to modeling choices. We therefore account for the systematic modeling error by adding it in quadrature to the statistical uncertainty (e.g., as shown in the magnification figures: Figures 1, 2, 3, 4, 5). We note that close to the critical curve, the deviation between models increases to above the few percent level quoted above, and it is approximately at the same level as the statistical error.

To evaluate how important these uncertainties are for studies of the background universe, we measure the extent of the field of view that is affected by high uncertainty. It is quantified in Figure 7. As these plots indicate, our models of RXC 0142, and Abell 2163 appear to be well-constrained throughout the field of view. Comparing the magnifications of model1, model2, and model3, we find that in 90% of the $200'' \times 200''$ field of view the models agree to better than 10%. In Abell 2537, 90% of the field of view is constrained to better than $\sim$ 25%. The extreme error test models (with significantly wrong redshift assumption) result in significant deviation and bias. However, even if an extreme redshift error was not noticed in the modeling process we still find that 90% of the field is constrained to better than 20-40%.

The case is different for ACT-CLJ0102 and RXC 2211. These two clusters appear to not have enough constraints, compared to the level of complexity of their mass distribution. The uncertainties of ACT-CLJ0102 are dominated by the statistical uncertainty, with a large range of magnification allowed by the lensing constraints. In RXC 2211, although we have spectroscopic confirmation of one of the sources, its low redshift and the fact that the small number of lensed galaxies come from only two source planes limits our ability to model this cluster with as high certainty as other clusters. In these two fields, the magnification uncertainty is less than 20% in approximately 60% of the field of view of RXC 2211, and 80% of the field of view of ACT-CLJ0102.

6. SUMMARY AND DISCUSSION

The main scientific goal of the RELICS program is to

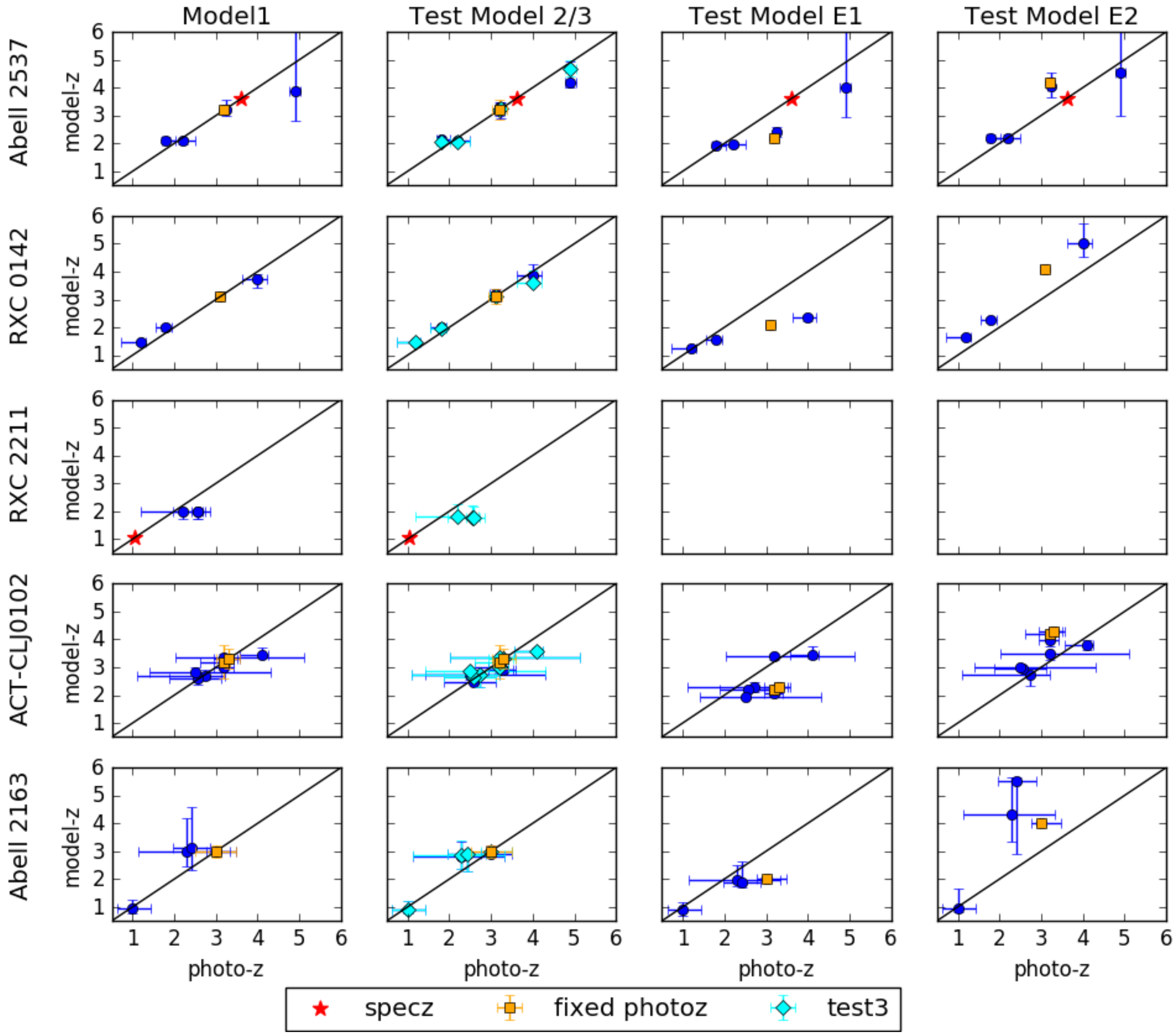

FIG. 6.— We plot the model-predicted redshifts against photometric redshifts for each of the test models considered in this paper. Model-z uncertainties (1σ) are from the MCMC sampling of the parameter space, and the photo-z uncertainties are from the BPZ photometric redshift analysis and represent the joint confidence limit marginalized over all the images of each system for which photo-z could be measured. Spectroscopic redshifts were always used as fixed parameters, and are labeled as 'specz' in the figure. Photometric redshifts that were used as fixed parameters are labeled as 'fixed'. A line with slope of unity is plotted in black to guide the eye. In tests E1 and E2, we deliberately fixed a redshift parameter to a redshift that is significantly lower or higher than its best photo-z, respectively. In these models, we find that the model systematically predicts other sources to have lower or higher redshifts when compared to their photo-zs, respectively, thus aiding in identifying whether a wrong redshift assumption was made. The two left panels show a reasonable agreement between the model-z and photo-z, confirming that the redshift assumptions that were used for these models produced reliable models, despite the small number of spectroscopic constraints. Tests E1 and E2 are not performed for RXC 2211 because its model did not use a photometric redshift as a fixed constraint.

TABLE 4
STRONG LENSING RESULTS

Cluster	M(< 300 kpc) [$10^{14} M_\odot$]	M(< 400 kpc) [$10^{14} M_\odot$]	M(< 500 kpc) [$10^{14} M_\odot$]	$R_E(z=3)$ [arcsec]	$R_E(z=9)$ [arcsec]	# sources (# clumps)	# spec-z
Abell 2537	2.0 ± 0.4	2.6 ± 0.5	···	28.6 ± 1.4	32.5 ± 1.6	4 (27)	1
RXC J0142.9+4438	3.4 ± 0.3	4.5 ± 0.4	···	30.1 ± 1.5	33.8 ± 1.7	4 (14)	0
RXCJ2211.7-0349	4.6 ± 0.2	6.3 ± 0.3	7.9 ± 0.4	47.2 ± 2.4	52.4 ± 2.6	3 (10)	1
ACT-CLJ0102-49151	5.7 ± 0.5	8.3 ± 0.6	11.0 ± 0.7	27.2 ± 1.4	40.3 ± 2.0	8 (28)	0
Abell 2163	1.6 ± 0.3	···	···	14.0 ± 0.7	14.9 ± 0.7	4 (12)	0

NOTE. — Strong lensing analysis summary by cluster. Lensing mass is projected mass density within a projected radius of 300, 400, and 500 kpc, centered on the BCG. Errors are 1σ and include model uncertainties. R_E is the effective Einstein radius, measured as $R_E = \sqrt{A/\pi}$, where A is the area enclosed in the tangential (outer) critical curve for a source at $z = 3.0$ and $z = 9.0$. We list the number of unique sources, as well as the total number of multiple images of clumps that were used as constraints in parentheses.

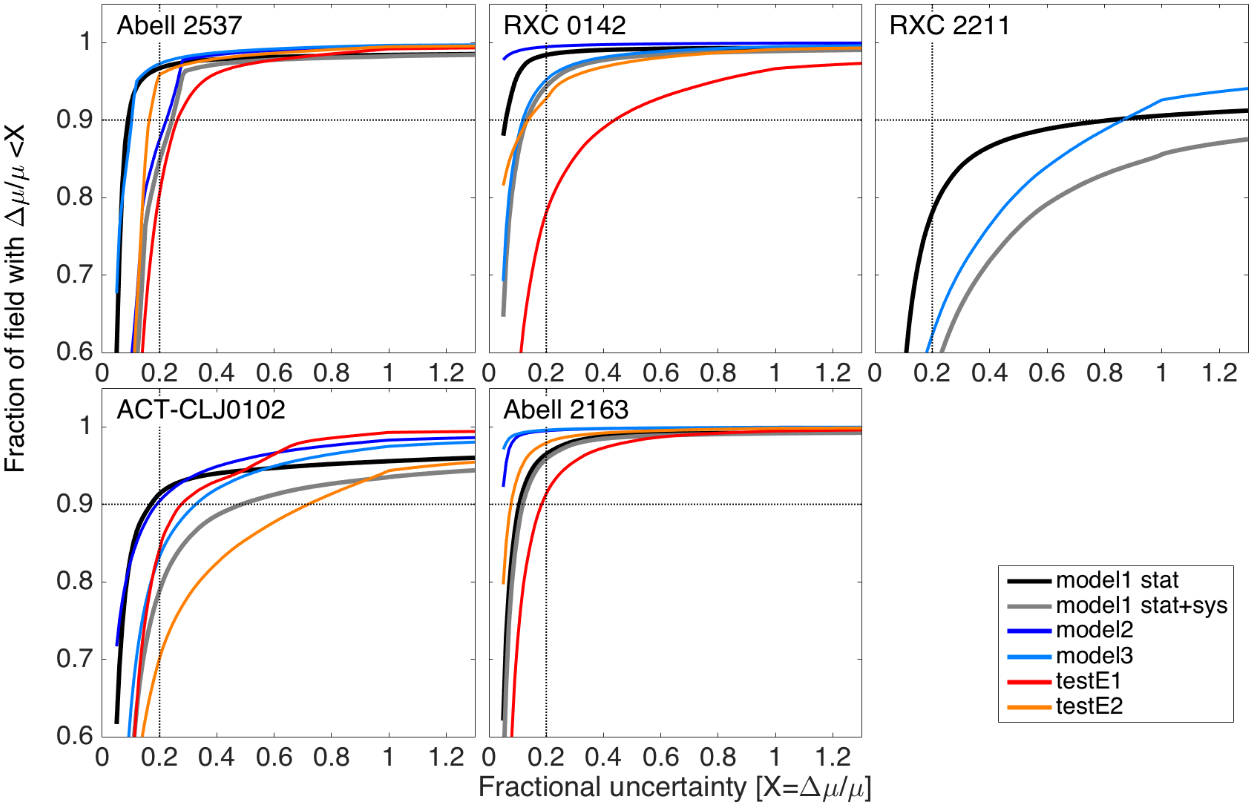

Fig. 7.— The fraction of the field in which the uncertainty (measured as $\Delta\mu/\mu$) is better (lower) than a given number. We show the statistical uncertainty in black, and the different uncertainty tests in colored lines as indicated in the legend. The models of testE1 and testE2 are extreme cases where the redshift is assumed to be significantly far from its best-fit value. The gray line adds in quadrature the statistical uncertainty and model2/3 uncertainty. Tests E1 and E2 are not performed for RXC 2211 because its model did not use a photometric redshift as a fixed constraint.

facilitate searches for high-redshift galaxies and constrain the luminosity function at the epoch of reionization. It is therefore most important to not only measure the magnification due to gravitational lensing in these fields, but to also provide a good understanding of the uncertainties – both statistical and systematic – related to the modeling process. In this paper, we present strong lensing models of the first five clusters out of the RELICS program. The model outputs are available to the community through the Mikulski Archive for Space Telescopes (MAST).

The accuracy of strong lens models relies on the availability of spectroscopic redshifts (e.g., Johnson & Sharon 2016), however, only two of the clusters considered here have spectroscopic measurements of background galaxies that can be used as model constraints. Given the available resources, we anticipate that a substantial fraction of the RELICS clusters will similarly not have spectroscopic redshift constraints prior to the first JWST call for proposals. We therefore devised a strategy to appropriately handle such cases. In Section 5 we detail our approach to minimize uncertainties due to lacking redshift constraints, and determine the reliability of lens models, by a careful incorporation of photometric redshift information into the lens modeling process.

At this stage, we lack spectroscopic redshifts for any multiple image set in ACT-CLJ0102-49151, Abell 2163, and RXC J0142.9+4438. The first two clusters have been targeted for spectroscopy by the RELICS program, however, we were unable to secure spectroscopic redshifts for any multiply-imaged sources that can constrain the models. If future observations secure spectroscopic redshifts for at least one multiply-imaged source in these fields, we will release revised lens models. Abell 2537 and RXC J2211.7-0349 have one spectroscopic redshift constraint each, as detailed in Section 4.

Our models for Abell 2537, RXC 0142, and RXCJ2211.7-0349 are the first to be published for these clusters.

We revisit the previously published strong-lensing model for ACT-CL0102 (Zitrin et. al 2013). With the new near-infrared data from WFC3/IR, we have deeper imaging data with broader wavelength coverage, which improves our ability to correctly identify multiply-imaged systems. The critical curves we derive from our model are thus slightly different than those presented in Zitrin et al. (2013), though the overall shape of the strong lensing model is similar. Although our new model is based on improved image identification, the lack of spectroscopic redshifts results in large statistical and systematic uncertainties on the lensing outputs ACT-CL0102, as can be seen in Figures 4 and 7. The complex mass distribution of ACT-CL0102-49151, the distribution of lensing constraints, and the flexibility of the redshift parameters result in degeneracies in the parameter space.

Spectroscopic redshifts of at least one system in each of the cluster cores of ACT-CL0102 will significantly reduce the lensing uncertainties. ACT-CL0102 is a high mass system that is likely going through a merger (Menanteau et al. 2012), and thus has a high cross section for lensing due to the increase in both shear and convergence (e.g., Zitrin et al. 2013). We confirm that the elongated shape of the lens model creates an extended region of high magnification across the cluster field (Figure 4).

Our work in this paper adds to previous work done for the cluster Abell 2163. Several weak lensing models have been published for this cluster (Squires et al. 1997, Cypriano et al. 2004, Radovich et al. 2008, Okabe et al. 2011). Our strong lensing analysis is limited to the north-eastern component of this system, as we only detect multiple images that provide strong lensing constraints in this region, though large distortion is evident in individual galaxies throughout the rest of the cluster field. Our strong lens model is only well constrained at the regions where strong lensing evidence is available.

We provide the effective Einstein radius for each cluster at redshifts $z = 3.0$ and $z = 9.0$ in Table 4. Table 4 also lists the projected mass density enclosed within radii of 300, 400, and 500 kpc from the BCG. The errors are derived from the uncertainty analysis in Section 5 added in quadrature to the statistical uncertainty from the MCMC sampling. Since at most only one spectroscopic redshift is available in each field, these models are limited in their ability to reliably measure the slope of the strong lensing mass. We do not include mass density measurements for Abell 2163 at radii greater than 300kpc because its strong lensing information is restricted to this area, and extrapolation out to larger radii will be inaccurate. Similarly, we only provide 500 kpc measurements for RXC 2211 and ACT-CL0102 because their elongated structure allows us to measure the mass density out to larger radii.

The photometric redshifts, which in RELICS are typically based on seven HST bands, provide important information and help reduce the uncertainties. Our uncertainty analysis indicates that the overall mass could have up to 10% bias (mass sheet degeneracy; e.g., Schneider & Seitz 1995) between our test models of Abell 2163, 20% in Abell 2537, >10% in RXC 0142, and 15% in ACT-CL0102. Unlike the other clusters, RXC 2211 has a limited number of lensing constraints. We detect lensed galaxies in two background source planes, only one of them spectroscopically confirmed. Our lensing analysis of this cluster indicates that it likely has a complex structure. With significantly fewer positional and redshift constraints compared to the other clusters, its model is less robust to changes in modeling assumptions. Both the lensing magnification and mass have higher uncertainty. The total projected mass density within a radius of $20 - 100''$ formally has low uncertainty of $< 5\%$, however, it shows large azimuthal and mass density slope variation between test models.

The "lensing efficiency" of a lens can be gauged by estimating the total magnified image-plane and source-plane area. A lens is considered more efficient when it lenses a larger area above a given magnification. Figure 8 shows the cumulative source plane area, for a source at $z = 9.0$, that is magnified above a given magnification, for all the clusters considered in this paper. We also show, in Figure 9, the effective source plane field of view that is captured by a $200'' \times 200''$ image in the direction of each cluster. We find that the lensing efficiency varies among clusters, and depends on the cluster redshift, elongation, and concentration, and thus is not a simple function of total cluster mass. To contextualize these clusters we compare their lensing efficiency to that of the clusters from the Frontier Fields program (shown in gray band in Figure 8, reproduced from Johnson et al.

2014). We find that most of the clusters presented here have comparable or somewhat lower lensing efficiency to those of the Frontier Fields clusters. Despite its high mass, Abell 2163 has a significantly lower lensing efficiency than other clusters, as can be seen in Figures 9 and 8. Its source plane is significantly less magnified, with most of the source plane area magnified by a less than a factor of 2. We speculate that this may be due to relatively low concentration. However, we leave an investigation of what causes this cluster to be a poor lens to future work; a proper analysis will benefit from a complete comparison set of lens models from the entire sample, as well as multi-wavelength measurements of its mass properties to derive mass estimates from other mass proxies.

The models presented in this paper represent a selection of the first galaxy clusters imaged by the RELICS survey. In the future, models will be computed for the remaining galaxy clusters that demonstrate strong lensing by using the same processes outlined here. These models will then be used to determine the intrinsic (unlensed) properties of magnified high-redshift galaxies by the RELICS collaboration and beyond. High level data products from the survey, including reduced images, catalogs, and lens models, will be made publicly available through MAST. The archive will be updated with improved version of the models in this paper, as well as other RELICS fields, with the acquisition of new data to support the lensing analysis.

This paper is based on observations made with the NASA/ESA Hubble Space Telescope, obtained at the Space Telescope Science Institute, which is operated by the Association of Universities for Research in Astronomy, Inc., under NASA contract NAS 5-26555. These observations are associated with program GO-14096. Archival data are associated with programs GO-9270, GO-12166, GO-12477, GO-12253. Support for program GO-14096 was provided by NASA through a grant from the Space Telescope Science Institute, which is operated by the Association of Universities for Research in Astronomy, Inc., under NASA contract NAS 5-26555. This paper includes data gathered with the 6.5 meter Magellan Telescopes located at Las Campanas Observatory, Chile. This work makes use of the Matlab Astronomy Package (Ofek 2014). F.A-S. acknowledges support from *Chandra* grant GO3-14131X.

REFERENCES

Applegate, D. E., von der Linden, A., Kelly, P. L., et al. 2014, MNRAS, 439, 48

Bleem, L. E., Stalder, B., de Haan, T., et al. 2015, ApJS, 216, 27

Bertin, E., & Arnouts, S. 1996, A&AS, 117, 393

Benítez, N. 2000, ApJ, 536, 571

Benitez, N., Dupke, R., Moles, M., et al. 2014, arXiv:1403.5237

Bradač, M., Clowe, D., Gonzalez, A. H., et al. 2006, ApJ, 652, 937

Bouwens, R. J., Illingworth, G. D., Oesch, P. A., et al. 2015, ApJ, 803, 34

Chirivì, G., Suyu, S. H., Grillo, C., et al. 2017, arXiv:1706.07815

Clowe, D., Bradač, M., Gonzalez, A. H., et al. 2006, ApJ, 648, L109

Coe, D., Benítez, N., Sánchez, S. F., et al. 2006, AJ, 132, 926

Cypriano, E. S., Sodré, L., Jr., Kneib, J.-P., & Campusano, L. E. 2004, ApJ, 613, 95

Ebeling, H., Stephenson, L. N., & Edge, A. C. 2014, ApJ, 781, L40

Fioc, M., & Rocca-Volmerange, B. 1997, A&A, 326, 950

Gladders, M. D., & Yee, H. K. C. 2000, AJ, 120, 2148

Gonzaga, S., & et al. 2012, The DrizzlePac Handbook, HST Data Handbook

Gruen, D., Seitz, S., Becker, M. R., Friedrich, O., & Mana, A. 2015, MNRAS, 449, 4264

Hasselfield, M., Hilton, M., Marriage, T. A., et al. 2013, J. Cosmology Astropart. Phys., 7, 008

Hoekstra, H., Herbonnet, R., Muzzin, A., et al. 2015, MNRAS, 449, 685

Johnson, T. L., Sharon, K., Bayliss, M. B., et al. 2014, ApJ, 797, 48

Johnson, T. L., & Sharon, K. 2016, ApJ, 832, 82

Jullo, E., Kneib, J.-P., Limousin, M., et al. 2007, New Journal of Physics, 9, 447

Limousin, M., Kneib, J.-P., & Natarajan, P. 2005, MNRAS, 356, 309

Lotz, J. M., Koekemoer, A., Coe, D., et al. 2017, ApJ, 837, 97

Mantz, A., Allen, S. W., Ebeling, H., Rapetti, D., & Drlica-Wagner, A. 2010, MNRAS, 406, 1773

Menanteau, F., Hughes, J. P., Sifón, C., et al. 2012, ApJ, 748, 7

Meneghetti, M., Natarajan, P., Coe, D., et al. 2016, arXiv:1606.04548

Ofek, E. O. 2014, Astrophysics Source Code Library, ascl:1407.005

Okabe, N., Bourdin, H., Mazzotta, P., & Maurogordato, S. 2011, ApJ, 741, 116

Piffaretti, R., Arnaud, M., Pratt, G. W., Pointecouteau, E., & Melin, J.-B. 2011, A&A, 534, A109

Planck Collaboration, Ade, P. A. R., Aghanim, N., et al. 2014, A&A, 571, A1

Planck Collaboration, Ade, P. A. R., Aghanim, N., et al. 2015, A&A, 582, A29

Planck Collaboration, Adam, R., Aghanim, N., et al. 2016, A&A, 596, A108

Postman, M., Coe, D., Benitez, N. et al., 2012, ApJS, 199, 25P

Radovich, M., Puddu, E., Romano, A., Grado, A., & Getman, F. 2008, A&A, 487, 55

Rafelski, M., Teplitz, H. I., Gardner, J. P., et al. 2015, AJ, 150, 31

Robertson, B. E. and Ellis, R. S. and Furlanetto, S. R. and Dunlop, J. S. 2015, ApJ, 802L, 19R

Rodney, S. A., Strolger, L.-G., Kelly, P. L., et al. 2016, ApJ, 820, 50

Sereno, M., & Ettori, S. 2015, MNRAS, 450, 3633

Schlafly, E. F., & Finkbeiner, D. P. 2011, ApJ, 737, 103

Schneider, P., & Seitz, C. 1995, A&A, 294, 411

Smith, G. P., Ebeling, H., Limousin, M., et al. 2009, ApJ, 707, L163

Squires, G., Neumann, D. M., Kaiser, N., et al. 1997, ApJ, 482, 648

Umetsu, K., Medezinski, E., Nonino, M., et al. 2014, ApJ, 795, 163

Umetsu, K., Zitrin, A., Gruen, D., et al. 2016, ApJ, 821, 116

von der Linden, A., Allen, M. T., Applegate, D. E., et al. 2014, MNRAS, 439, 2

Wen, Z. L., Han, J. L., & Liu, F. S. 2012, ApJS, 199, 34

Wright, E. L., Eisenhardt, P. R. M., Mainzer, A. K., et al. 2010, AJ, 140, 1868-1881

Wong, K. C., Zabludoff, A. I., Ammons, S. M., et al. 2013, ApJ, 769, 52

Wuyts, S., Labbé, I., Förster Schreiber, N. M., et al. 2008, ApJ, 682, 985-1003

Zitrin, A., Menanteau, F., Hughes, J. P., et al. 2013, ApJ, 770, L15

Zitrin, A., Fabris, A., Merten, J., et al. 2015, ApJ, 801, 44

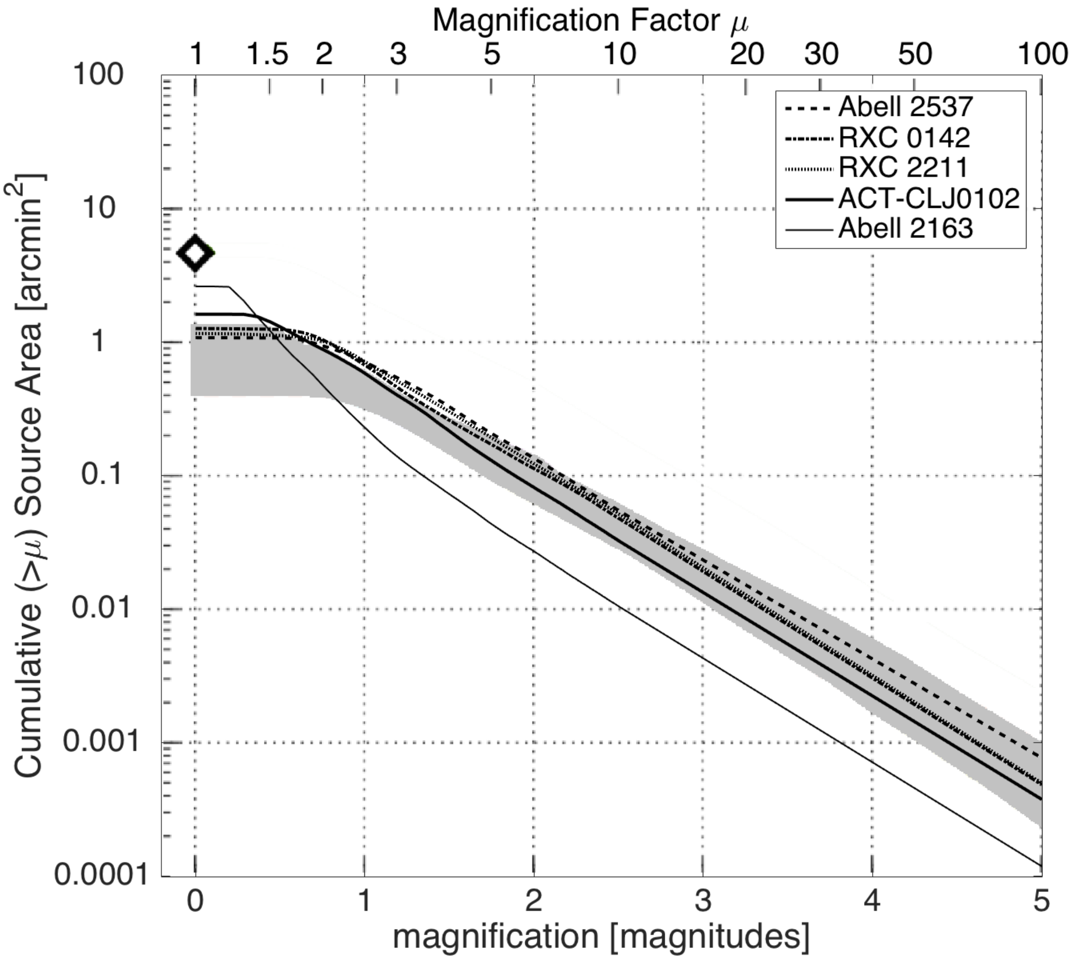

Fig. 8.— The cumulative source plane area with magnification higher than a given number, for a source at $z = 9.0$. For all the clusters, we assume an image plane field of view of $130'' \times 130''$, which is approximately the field of view of the WFC3/IR camera. We show the corresponding area of one WFC3/IR FOV with the black diamond. The shaded gray band represents the range of lensing efficiencies for the six clusters from the *HST* Frontier Fields program (Lotz et al. 2017), reproduced from Johnson et al. (2014). We plot the lensing efficiencies for the five clusters presented in this paper on top of this band. All efficiencies are plotted for the source plane.

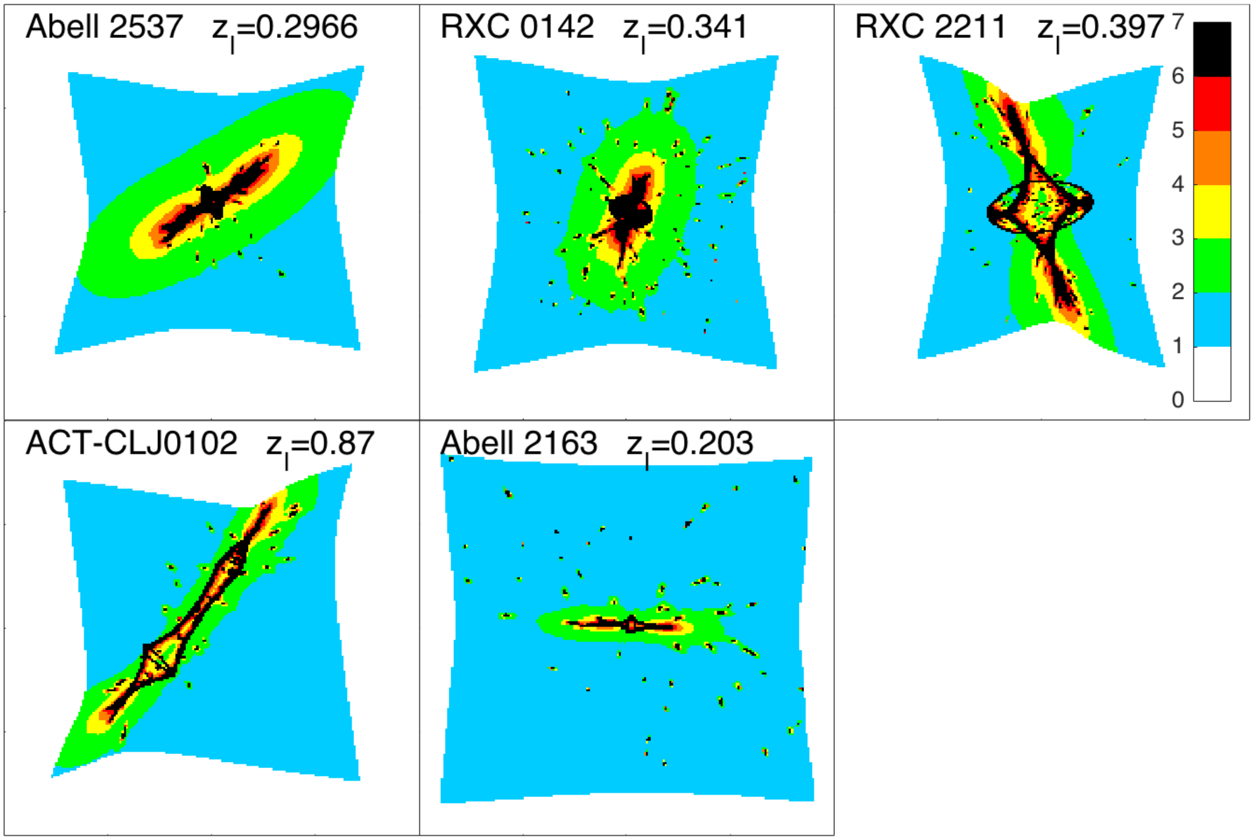

Fig. 9.— The $z = 9.0$ source plane, color coded by magnification, to show the lensing efficiency of each cluster. Each box is $200'' \times 200''$ approximately the field of view of ACS. The $200'' \times 200''$ image plane was ray-traced to the source plane using the best-fit model1 of each cluster. Except for ACT-CL0102, all fields are centered on the BCG.

TABLE 5
Abell 2537 – Properties of lensed galaxies

ID	R.A.	Decl.	Photo-z [$z_{min} - z_{max}$]	Spec-z	Model-z	rms (")
1.1	23:08:21.468	-02:11:19.17	0.40 [0.34–0.50]	-	$2.16^{+0.13}_{-0.15}$	0.52
1.2	23:08:23.244	-02:11:35.70	1.83 [1.79–1.95]	-		
1.3	23:08:21.103	-02:11:56.49	1.88 [1.74–2.03]	-		
1.4	23:08:23.114	-02:11:03.16	1.80 [1.70–1.93]	-		
12.1	23:08:21.52	-02:11:19.84	1.41 [0.20–3.09]	-	$2.12^{+0.16}_{-0.12}$	0.60
12.2	23:08:23.333	-02:11:35.73	2.49 [2.20–2.65]	-		
12.3	23:08:21.197	-02:11:57.50	0.84 [0.18–3.40]	-		
12.4	23:08:23.258	-02:11:04.73	2.25 [1.33–2.68]	-		
2.1	23:08:23.738	-02:11:23.46	3.95 [3.83–4.06]	-	-	0.65
2.2	23:08:23.494	-02:11:10.57	3.81 [3.65–3.96]	-	-	
2.3	23:08:21.802	-02:11:16.51	3.82 [3.64–3.98]		-	
2.4	23:08:22.231	-02:11:24.58	3.74 [3.57–3.91]	3.611	-	
20.1	23:08:23.681	-02:11:14.42	-	-	$3.48^{+0.27}_{-0.14}$	0.90
20.2	23:08:23.609	-02:11:12.72	-	-		
20.3	23:08:21.878	-02:11:17.67	-	-		
20.4	23:08:22.162	-02:11:22.03	-	-		
3.1	23:08:19.870	-02:11:19.01	3.25 [3.19–3.31]	-	[3.2]	0.83
3.2	23:08:19.666	-02:11:25.42	3.22 [3.13–3.27]	-		
3.3	23:08:21.132	-02:10:54.45	3.24 [3.16–3.29]	-		
31.1	23:08:19.850	-02:11:19.93	-	-	$3.25^{+0.41}_{-0.20}$	0.71
31.2	23:08:19.694	-02:11:24.60	-	-		
31.3	23:08:21.276	-02:10:53.20	2.69 [2.57–2.76]	-		
32.1	23:08:19.860	-02:11:19.63	-	-	$3.29^{+0.46}_{-0.30}$	0.61
32.2	23:08:19.685	-02:11:24.91	-	-		
32.3	23:08:21.235	-02:10:53.57	-	-		
4.1	23:08:20.640	-02:11:35.45	4.86 [4.76–5.03]	-	$4.80^{+2.43}_{-2.17}$	0.26
4.2	23:08:20.666	-02:11:39.74	4.93 [4.81–5.01]	-		

Note. — Properties of the images that were used as constraints in the lens model of Abell 2537. The model-z and rms are given for the best-fit model, and the rms is measured in the image plane for each family of multiple images.

TABLE 6
Abell 2537 Model Parameters

ID	ΔR.A. (")	ΔDecl. (")	ϵ	θ (°)	r_{core} (")	r_{cut} (")	σ (km s^{-1})
Halo 1	$7.65^{+6.69}_{-9.03}$	$19.20^{+5.43}_{-12.56}$	$0.57^{+0.20}_{-0.17}$	$215.98^{+2.72}_{-2.09}$	$65.32^{+29.21}_{-19.28}$	[339]	1100^{+251}_{-119}
Halo 2	$-0.04^{+0.68}_{-0.61}$	$0.56^{+1.19}_{-1.10}$	$0.28^{+0.08}_{-0.05}$	$21.91^{+4.09}_{-5.00}$	$10.18^{+1.20}_{-1.15}$	270^{+129}_{-135}	861^{+54}_{-69}

Note. — Parameters for the best-fit lens model of Abell 2537. Error bars correspond to 1σ confidence level as inferred from the MCMC optimization. ΔR.A. and ΔDecl. are defined in relation to the center of the seventh-brightest cluster galaxy in the field, which is identified as the BCG, located at *R.A.*=16:15:48.948 and *Decl.*=-06:08:41.38. Position angles are measured north of west, and the ellipticity ϵ is defined as $(a^2 - b^2)/(a^2 + b^2)$. Square brackets indicate fixed parameters. r_{cut} is fixed to 1500kpc for Halo 1.

TABLE 7
RXC J0142.9+4438 – Properties of lensed galaxies

ID	R.A.	Decl.	Photo-z [$z_{min} - z_{max}$]	Spec-z	Model-z	rms (")
1.1	01:42:55.250	+44:38:26.97	1.80 [1.55–1.86]	-	$1.99^{+0.10}_{-0.10}$	0.25
1.2	01:42:52.212	+44:37:51.41	1.81 [1.73–1.94]	-		
1.3	01:42:57.138	+44:37:53.30	0.20 [0.16–0.25]	-		
1.4	01:42:57.460	+44:38:08.00	0.11 [0.05–0.15]	-		
2.1	01:42:53.869	+44:38:27.13	1.01 [0.72–1.10]	-	$1.46^{+0.07}_{-0.06}$	0.61
2.2	01:42:52.976	+44:38:20.35	-	-		
2.3	01:42:56.811	+44:38:27.42	1.19 [1.15–1.31]	-		
3.1	01:42:52.684	+44:38:08.64	3.11 [3.02–3.23]	-	[3.1]	0.44
3.2	01:42:52.771	+44:38:10.32	3.17 [3.06–3.24]	-		
3.3	01:42:54.168	+44:37:43.53	3.10 [2.98–3.22]	-		
3.4	01:42:58.386	+44:38:20.99	3.25 [0.15–3.66]	-		
4.1	01:42:55.725	+44:38:33.72	0.44 [0.10–0.66]	-	$3.71^{+0.22}_{-0.29}$	0.04
4.2	01:42:56.835	+44:38:28.23	0.45 [0.18–3.93]	-		
4.3	01:42:56.864	+44:37:48.19	4.05 [3.63–4.21]	-		

Note. — Properties of the images that were used as constraints in the lens model of RXC J0142.9+4438. The model-z and rms are given for the best-fit model, and the rms is measured in the image plane for each family of multiple images.

TABLE 8

RXC J0142.9+4438 MODEL PARAMETERS

Object	ΔR.A. (”)	ΔDecl. (”)	ϵ	θ (°)	r_{core} (”)	r_{cut} (”)	σ (km s^{-1})
Halo 1	$2.18^{+0.10}_{-0.11}$	$1.06^{+0.09}_{-0.13}$	$0.23^{+0.02}_{-0.02}$	$70.25^{+0.34}_{-0.61}$	$12.93^{+1.41}_{-1.52}$	[309]	1148^{+22}_{-22}

NOTE. — Parameters for the best-fit model of the halo in RXC J0142.9+4438. Error bars correspond to 1σ confidence level as inferred from the MCMC optimization. ΔR.A. and ΔDecl. are defined in relation to the center of the seventh-brightest cluster galaxy in the field, which serves as the BCG for our lens model. The BCG is located at *R.A.* = 1:42:55.230 and *Decl.* = +44:38:04.63. Position angles are measured north of west, and the ellipticity ϵ is defined as $(a^2 - b^2)/(a^2 + b^2)$. Square brackets indicate fixed parameters. r_{cut} is fixed to 1500kpc for Halo 1.

TABLE 9

RXC J2211.7-0349 – PROPERTIES OF LENSED GALAXIES

ID	R.A.	Decl.	Photo-z [$z_{min} - z_{max}$]	Spec-z	Model-z	rms (”)
1.1	22:11:45.605	-03:49:26.62	0.82 [0.71–0.89]	1.051	-	0.12
1.2	22:11:43.927	-03:49:43.70	0.83 [0.73–0.94]	-	-	
1.3	22:11:45.245	-03:50:03.50	0.85 [0.71–0.94]	-	-	
1.4	22:11:48.564	-03:49:52.38	0.53 [0.42–0.63]	-	-	
1.5	22:11:45.797	-03:49:44.44	-	-	-	
2.1	22:11:43.457	-03:50:12.02	2.41 [1.96–2.60]	-	$1.80^{+0.19}_{-0.07}$	0.28
2.2	22:11:44.256	-03:50:21.08	2.59 [2.40–2.72]	-		
2.3	22:11:48.835	-03:50:17.57	2.72 [2.43–2.85]	-		
3.1	22:11:43.560	-03:50:10.02	2.42 [1.81–2.69]	-	$1.83^{+0.19}_{-0.08}$	0.35
3.2	22:11:44.172	-03:50:17.55	1.78 [1.69–2.08]	-		
3.3	22:11:49.054	-03:50:13.57	2.40 [1.20–2.67]	-		

NOTE. — Properties of the images that were used as constraints in the lens model of RXC J2211.7-0349. The model-z and rms are given for the best-fit model, and the rms is measured in the image plane for each family of multiple images.

TABLE 10

RXC J2211.7-0349 MODEL PARAMETERS

Object	ΔR.A. (”)	ΔDecl. (”)	ϵ	θ (°)	r_{core} (”)	r_{cut} (”)	σ (km s^{-1})
Halo 1	$2.51^{+2.97}_{-2.81}$	$-0.62^{+5.50}_{-3.71}$	$0.68^{+0.11}_{-0.11}$	$103.54^{+3.96}_{-1.88}$	$36.37^{+11.56}_{-8.52}$	[280]	1362^{+122}_{-116}
Halo 2	$-1.66^{+2.17}_{-1.43}$	$-1.74^{+0.77}_{-0.45}$	$0.21^{+0.36}_{-0.07}$	$64.78^{+21.19}_{-9.49}$	$6.97^{+1.96}_{-4.34}$	115^{+66}_{-46}	898^{+97}_{-143}

NOTE. — Parameters for the best-fit model of the halo in RXC J2211.7-0349. Error bars correspond to 1σ confidence level as inferred from the MCMC optimization. ΔR.A. and ΔDecl. are defined in relation to the center of the seventh-brightest cluster galaxy in the field, which serves as the BCG for our lens model. The BCG is located at *R.A.* = 22:11:45.928 and *Decl.* = -3:49:44.25. Position angles are measured north of west, and the ellipticity ϵ is defined as $(a^2 - b^2)/(a^2 + b^2)$. Square brackets indicate fixed parameters. r_{cut} is fixed to 1500kpc for Halo 1.

TABLE 11
ACT-CLJ0102-49151 – Properties of lensed galaxies

ID	R.A.	Decl.	Photo-z $[z_{min} - z_{max}]$	Spec-z	Model-z	rms (")
1.1	01:02:53.478	-49:15:16.01	0.41 [0.11–4.06]	-	$3.01^{+0.13}_{-0.09}$	0.37
1.2	01:02:52.604	-49:15:19.68	0.35 [0.30–0.39]	-		
1.3	01:02:55.321	-49:15:01.20	0.33 [0.30–3.49]	-		
10.1	01:02:53.328	-49:15:16.38	3.39 [0.22–3.50]	-	[3.00]	0.90
10.2	01:02:52.758	-49:15:18.72	2.69 [2.48–2.83]	-		
10.3	01:02:55.389	-49:15:00.33	3.13 [2.89–3.31]	-		
2.1	01:02:55.976	-49:15:51.25	3.35 [3.18–3.50]	-	[3.3]	0.66
2.2	01:02:56.571	-49:15:47.12	3.37 [3.20–3.51]	-		
2.3	01:02:54.461	-49:16:03.69	3.14 [2.89–3.28]	-		
20.1	01:02:55.831	-49:15:52.37	3.26 [3.07–3.54]	-	[3.3]	0.29
20.2	01:02:56.741	-49:15:45.98	3.09 [2.90–3.26]	-		
20.3	01:02:54.403	-49:16:04.52	3.44 [3.28–3.54]	-		
3.1	01:02:56.255	-49:15:07.05	4.40 [4.27–4.47]	-	$7.68^{+0.30}_{-1.03}$	0.24
3.2	01:02:54.741	-49:15:19.56	4.21 [3.99–4.34]	-		
3.3	01:02:51.532	-49:15:38.47	4.56 [4.45–4.64]	-		
4.1	01:02:55.349	-49:16:26.10	4.05 [3.87–4.15]	-	$3.46^{+0.23}_{-0.09}$	0.26
4.2	01:02:59.982	-49:15:49.54	4.16 [3.93–4.24]	-		
4.3	01:02:56.593	-49:16:08.27	4.05 [3.56–4.18]	-		
5.1	01:03:00.154	-49:16:03.37	2.53 [1.98–2.72]	-	$3.34^{+0.16}_{-10}$	0.20
5.2	01:02:55.763	-49:16:41.04	0.34 [0.27–3.36]	-		
8.1	01:02:58.731	-49:16:35.79	2.73 [0.24–3.21]	-	$2.70^{+0.21}_{-0.14}$	0.20
8.2	01:02:58.512	-49:16:37.03	1.13 [1.10–2.56]	-		
9.1	01:02:55.632	-49:16:17.53	2.57 [2.25–2.77]	-	$2.60^{+0.21}_{-0.24}$	0.46
9.2	01:02:56.294	-49:16:07.72	2.73 [2.52–3.10]	-		
9.3	01:02:59.057	-49:15:53.21	2.35 [1.86–2.84]	-		
13.1	01:02:54.528	-49:14:58.65	2.48 [2.09–2.97]	-	$2.82^{+0.16}_{-0.05}$	0.16
13.2	01:02:53.246	-49:15:06.98	4.60 [4.20–4.99]	-		
13.3	01:02:51.806	-49:15:17.03	2.47 [2.16–2.70]	-		

Note. — Properties of the images that were used as constraints in the lens model of ACT-CLJ0102-49151. The model-z and rms are given for the best-fit model, and the rms is measured in the image plane for each family of multiple images.

TABLE 12
ACT-CLJ0102-49151 Model Parameters

Object	ΔR.A. (")	ΔDecl. (")	ϵ	θ (°)	r_{core} (")	r_{cut} (")	σ (km s^{-1})
Halo 1	$44.47^{+0.29}_{-0.33}$	$72.65^{+0.57}_{-0.61}$	$0.94^{+0.02}_{-0.02}$	$63.76^{+2.39}_{-1.77}$	$1.37^{+0.55}_{-1.29}$	[194]	826^{+42}_{-60}
Halo 2	$-7.13^{+2.35}_{-1.16}$	$-1.50^{+1.90}_{-1.23}$	$0.58^{+0.11}_{-0.13}$	$43.36^{+1.48}_{-0.91}$	$10.22^{+3.30}_{-3.18}$	368^{+20}_{-76}	1064^{+90}_{-62}

Note. — Parameters for the best-fit model of the halo in ACT-CLJ0102-49151. Error bars correspond to 1σ confidence level as inferred from the MCMC optimization. ΔR.A. and ΔDecl. are defined in relation to the center of the seventh-brightest cluster galaxy in the field, which serves as the BCG for our lens model. The BCG is located at *R.A.* = 1:02:57.769 and *Decl.* = -49:16:19.20. Position angles are measured north of west, and the ellipticity ϵ is defined as $(a^2 - b^2)/(a^2 + b^2)$. Square brackets indicate fixed parameters. r_{cut} is fixed to 1500kpc for Halo 1.

TABLE 13
Abell 2163 – Properties of lensed galaxies

ID	R.A.	Decl.	Photo-z $[z_{min} - z_{max}]$	Spec-z	Model-z	rms (")
1.1	16:15:48.655	-06:08:47.34	3.10 [2.89–3.26]	-	[3.00]	0.11
1.2	16:15:48.825	-06:08:50.00	2.90 [2.77–3.09]	-		
1.3	16:15:48.773	-06:08:20.14	0.34 [0.23–3.49]	-		
2.1	16:15:48.578	-06:08:46.90	-	-	$3.00^{+1.17}_{-0.56}$	0.05
2.2	16:15:48.806	-06:08:51.06	2.97 [2.36–3.33]	-		
2.3	16:15:48.742	-06:08:20.95	1.69 [1.13–2.74]	-		
3.1	16:15:49.372	-06:08:36.03	2.36 [2.22–2.73]	-	$3.14^{+1.37}_{-0.81}$	0.18
3.2	16:15:49.062	-06:08:58.98	2.26 [1.97–2.69]	-		
3.3	16:15:48.900	-06:08:27.96	2.65 [2.20–2.87]	-		
4.1	16:15:47.244	-06:08:39.74	0.77 [0.45–0.92]	-	$0.93^{+1.32}_{-0.17}$	0.16
4.2	16:15:47.203	-06:08:41.15	0.53 [0.44–0.68]	-		
4.3	16:15:47.280	-06:08:45.78	1.14 [1.09–1.24]	-		

Note. — Properties of the images that were used as constraints in the lens model of Abell 2163. The model-z and rms are given for the best-fit model, and the rms is measured in the image plane for each family of multiple images.

TABLE 14

Abell 2163 Model Parameters

Object	ΔR.A. (")	ΔDecl. (")	ϵ	θ (°)	r_{core} (")	r_{cut} (")	σ (km s^{-1})
Halo 1	$3.82^{+5.98}_{-2.04}$	$1.09^{+0.39}_{-1.02}$	$0.73^{+0.14}_{-0.25}$	$179.13^{+1.25}_{-1.68}$	$14.71^{+11.46}_{-2.88}$	[449]	750^{+140}_{-36}
Halo 2	[-0.687]	[0.911]	$0.47^{+0.20}_{-0.46}$	$0.18^{+9.52}_{-0.05}$	$14.71^{+11.46}_{-2.88}$	97^{+79}_{-81}	425^{+14}_{-109}

Note. — Parameters for the best-fit model of the halo in Abell 2163. Error bars correspond to 1σ confidence level as inferred from the MCMC optimization. ΔR.A. and ΔDecl. are defined in relation to the center of the seventh-brightest cluster galaxy in the field, which serves as the BCG for our lens model. The BCG is located at *R.A.* = 16:15:48.948 and *Decl.* = -06:08:41.38. Position angles are measured north of west, and the ellipticity ϵ is defined as $(a^2 - b^2)/(a^2 + b^2)$. r_{cut} is fixed to 1500kpc for Halo 1.